



Technical University of Crete

School of Production Engineering and Management

Division of Production Systems

Turbomachines and Fluid Dynamics Laboratory

Graphical User Interface Development for a Wind Turbine Analysis Software

By

Maria I. Seremeti

Diploma Thesis

Supervisor

Dr. Ioannis K. Nikolos, Professor

Chania, October 2019

Copyright© Maria I. Seremeti, 2019.
All rights reserved.



Technical University of Crete

School of Production Engineering and Management

Division of Production Systems

Turbomachines and Fluid Dynamics Laboratory

Graphical User Interface Development for a Wind Turbine Analysis Software

By

Maria I. Seremeti

Approved by:

Dr. Ioannis K. Nikolos

Professor

Technical University of Crete
School of Production Engineering
& Management

Dr. Anargyros I. Delis

Associate Professor

Technical University of Crete
School of Production Engineering
& Management

Dr. Fotios D. Kanellos

Assistant Professor

Technical University of Crete
School of Production Engineering
& Management

Date Defended: 08 October 2019

Abstract

Over the past years, several mathematical models have been proposed for the aerodynamic response analysis and power output prediction of wind turbine rotors. Among them, the BEM theory is considered as the current standard for assessing the rotor performance in design and aero-elastic analysis applications, given its ability to obtain remarkably accurate results for a wide range of operating conditions, in a very short period of time. This diploma thesis presents the development of a new Graphical User Interface (GUI) for the support of a BEM analysis software (BEMcode), previously developed in the Turbomachines and Fluid Dynamics Laboratory (TurboLab – TUC) at the School of Production Engineering and Management of Technical University of Crete. The current GUI implementation was accomplished by the utilization of C++ programming language and Qt cross-platform application. The user is able to utilize different data input methods, as well as to visualize and extract the corresponding results. The particular GUI allows for the convenient generation of the preferred airfoils, the calculation of the required aerodynamic coefficients (by incorporating XFOIL solver), the extrapolation of the lift and drag coefficients to the whole 360° range of angles of attack, as well as the definition and visualization of the blade geometry. During the BEM simulation the user is able to include several correction models that increase the accuracy of BEM theory, while the simulation of shrouded or Diffuser Augmented Wind Turbine (DAWT) rotors is also available, through the incorporation of an extended 1D Momentum theory. The accuracy of BEMcode software was successfully assessed against the well-known QBlade software, as well as against numerical and experimental data available in the literature.

Acknowledgements

First and foremost, I would like to express my deepest gratitude to my advisor, Professor Ioannis K. Nikolos, for his trust by assigning to me this project. Since the early years of my undergraduate studies I wished to collaborate with Dr. Ioannis K. Nikolos and contribute to his work. His motivation gave me greater motivation. His patience, knowledge and continuous support helped me to stay focused during all time in order this thesis to be accomplished. I could have never imagined a better advisor.

Also, I would like to express my sincere gratitude to the PhD candidate Stavros N. Leloudas for all his contribution. His willingness, support and constant guidance were the source of motivation for me. It was a very pleasant collaboration during all time.

I would like to express my gratitude to my beloved family and closest friends, who supported me and stayed by my side.

But most importantly of all, I would like to express all my love and gratitude to my mother, Stella, for her unconditional love, support, patience and everything that she has done all these years, in order me to be at this level at the moment. None of these would have happened without her. This diploma thesis is dedicated to her.

Contents

Abstract	4
Acknowledgements	5
List of Symbols	8
Abbreviations	9
Chapter 1 – Introduction	10
1.1 Wind Energy	10
1.2 Aerodynamics in Wind Turbine Design	12
1.3 Principles of Horizontal Axis Wind Turbine Aerodynamics	14
1.4 The Diffuser-Augmented Wind Turbine.....	16
1.4.1 Wind Force Mechanism	18
1.4.2 Mixing of the Wake and the External Flow Mechanism	19
1.5 Current Status of Aerodynamic Design Models.....	19
1.6 The Structure of the Diploma Thesis	20
Chapter 2 – The Blade Element Momentum Theory	22
2.1 Overview.....	22
2.2 The 1D Momentum Theory	23
2.2 The Classical BEM Model.....	26
2.3 The Diffuser Effect on the 1D Momentum Theory	28
2.4 The Modified Blade Element Momentum Model	31
2.5 Correction Models	32
2.5.1 The Prandtl’s Correction Model.....	33
2.5.2 The Glauert’s correction model	34
2.5.3 The Shen’s correction model.....	36
2.6 The Iterative Scheme.....	37
2.7 The Relaxation Factor	38
Chapter 3 – The BEMcode Software	40
3.1 BEMcode Software Overview	40
3.1.1 About Qt.....	40
3.2 Main Window	40
3.3 Airfoil Dialog	42
3.4 XFOIL Analysis Dialog.....	53
3.5 360° Extrapolation Dialog.....	59
3.6 Blade Creation Dialog.....	63

3.7 BEM Simulation Dialog.....66

Chapter 4 – Validation.....71

4.1 Case I: NREL Phase VI Blade71

 4.1.1 Case I: Results72

4.2 Case II: NREL 5MW75

 4.2.1 Case II: Results.....77

4.3 Case III: The DAWT of Donqi Urban Windmills.....79

 4.3.1 Case III: Results81

Chapter 5 – Conclusions.....83

References84

List of Symbols

Latin Symbols

T	Thrust [N]
M	Torque [$N \cdot m$]
L	Lift force [N]
D	Drag force [N]
P_n	Normal force [N]
P_t	Tangential force [N]
C_l	Lift coefficient [–]
C_d	Drag coefficient [–]
C_m	Moment coefficient [–]
C_n	Normal force coefficient [–]
C_t	Tangential force coefficient [–]
C_P	Power coefficient [–]
C_T	Thrust coefficient [–]
V_o	Freestream Velocity [m/s]
u	Axial component of the velocity on the rotor plane [m/s]
u_1	Axial component of the velocity in the wake [m/s]
C_θ	Rotational velocity in the wake [rad/s]
V_{rel}	Relative velocity [m/s]
F	Prandtl's correction factor
F_S	Shen's correction factor
N	Number of blade elements
c	Blade chord [m]
B	Number of blades [–]
R_{tip}	Blade Tip Radius [m]
R_{hub}	Hub Radius [m]
\dot{m}	Mass flow rate [kg/s]
n_d	Diffuser efficiency [–]
c_p	Pressure coefficient [–]

Greek Symbols

α_a	Axial induction factor [–]
α_t	Tangential induction factor [–]
α	Angle of attack [<i>deg</i>]
α_a^d	Axial induction factor for the case of a DAWT [–]
α_t^d	Tangential induction factor for the case of a DAWT [–]
ω	Rotational speed of the rotor [<i>rad/s</i>]
θ	Twist angle [<i>deg</i>]
ϕ	Inflow angle [<i>deg</i>]
λ	Tip-speed ratio [–]
σ	Rotor solidity [–]
ρ	Density of air [<i>kg/m³</i>]
ν	Kinematic viscosity of air [<i>m²/s</i>]
ε	Velocity speed-up ratio at the rotor plane [–]
γ	Velocity speed-up ratio at the rotor plane for an unloaded diffuser [–]

Abbreviations

APE	Annual Produced Energy
ATC	Annual Total Cost
BEM	Blade Element Momentum
CFD	Computational Fluid Dynamics
DAWT	Diffuser-Augmented Wind Turbine
GUI	Graphical User Interface
HAWT	Horizontal-Axis Wind Turbine
LCoE	Levelized Cost-of-Energy
OECD	Organization for Economic Cooperation and Development
TSR	Tip-Speed Ratio
WHO	World Health Organization

Chapter 1 – Introduction

1.1 Wind Energy

Growth in the worldwide population and economy – coupled with rapid urbanization and social developments – are expected to result in a substantial increase of energy demand over the future years. According to the recent estimates and projections issued by the Department of Economic and Social Affairs of the United Nations Secretariat, the global population is about to rise from 7.6 billion in 2017 to 9.8 billion by 2050 [UN19]. In addition, the process of urbanization – which currently adds a city with approximately the size of Shanghai to the urban population of the world every four months – will eventually result in two-thirds of the world's people living in urban areas by 2050; that figure represents a growth of 54 percent, comparatively to 2014. Accordingly, energy consumption on a global scale is expected to increase by 27 percent until 2040 [WE018]. That growth is estimated to predominantly come from countries that are not members of the Organization for Economic Cooperation and Development (OECD) and mostly from those driven by high economic growth. In particular, Asia is anticipated to experience the largest demand growth, in comparison with the rest of the world. By 2040, the Asia Pacific region will consume 46 percent of the world's energy [WE018]. Consequently, meeting the rapidly growing energy demand, while reducing the harmful emissions of greenhouse gases, stands among the most significant, but also challenging, problems of our times.

Aside from the challenges of meeting the rising energy demand and mitigating climate change, cleaner air is a vital need. According to the World Health Organization (WHO), air pollution is the world's largest environmental risk. In 2018, the global atmospheric concentrations of carbon dioxide rose by 1.7 percent, as compared to the previous year. That annual rise, which is the largest one ever recorded, pushed carbon emissions to a landmark high of 33 billion tons. WHO estimates that in 2012, about seven million people died prematurely as a result of air pollution, many of these either from industrial sources, such as power generation, or from indoor air pollution, which could be averted by electricity use. At the same time, climate change is not just an environmental hazard but also an economic threat; rising sea levels, more severe droughts and health issues will increase insurance costs radically in the future [Ton07].

Wind energy is one of the most effective and promising power technologies that are ready today to be deployed globally on a scale that can contribute in tackling these problems. Wind energy represents a sustainable and ecofriendly resource, being at the same time safe and abundant. In this context, since 1980, the size of wind turbines increased rapidly from about 17 m in diameter with a nominal capacity of 75 kW to about 125 m in diameter with a capacity reaching 5 MW, as shown in

Figure 1.1. Besides, the initial capital cost of wind turbines has also been significantly reduced. A number of assessments confirm that the world's wind resources are enormous and well distributed. The total available resource that is technically recoverable is estimated to be 53,000 TWh/year, which will be over twice as large as the projection for the world's entire electricity demand in 2020. In addition, annual wind power installations in Europe have increased more or less steadily over the past 11 years, from 6.7 GW in 2005 to 13.9 GW in 2016. 2017 has been a record year, since 16.8 GW came online. At the end of June 2018, Europe had a total of 182 GW of wind power capacity installed (comprised by 165 GW onshore and 16.9 GW offshore installations). Today, Germany remains the market leader in Europe, followed by Spain, United Kingdom, France and Italy. Five other European countries (namely, Turkey, Sweden, Poland, Denmark and Portugal) have more than 5 GW installed. Eight additional European countries (Austria, Belgium, Finland, Greece, Ireland, the Netherlands, Norway and Romania) have over 1 GW of installed capacity [Ton07].

Lack of resource is therefore unlikely to be a barrier to the penetration of wind technology in the energy market. However, cost is a major barrier, since wind energy has to face high competition from conventional sources of energy based on fossil-fuels and nuclear energy. Despite the great progress made, wind energy still has a long way to go before it reaches its full potential in terms of the large-scale supply of electricity. While it can already be cost-competitive with newly built conventional plants, at sites with good wind speeds, further cost reductions are necessary [Ton07].

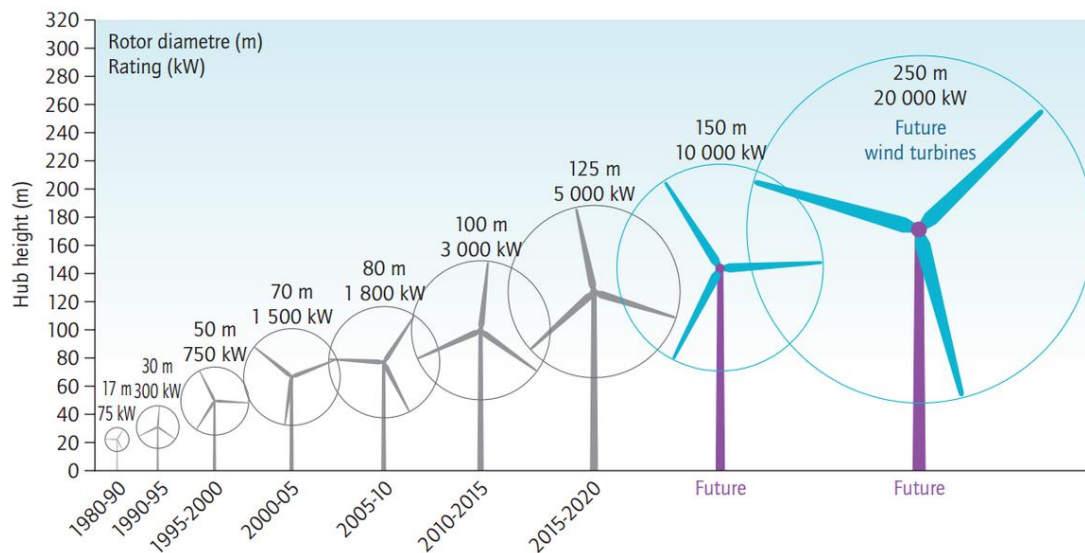


Figure 1.1: Growth in size of wind turbines since 1980 [IEA].

Research and development could contribute up to 40 percent of those reductions. The challenge faced by the wind energy community is to produce more cost-competitive wind turbines through highly optimized designs.

1.2 Aerodynamics in Wind Turbine Design

Wind turbine is known to be one complex system working in a complex environment. It means that wind turbines should be functional in various geographical sites, in which different kinds of meteorological phenomena and topographical features prevail. In view of that, the design of a wind turbine is a difficult and complicated procedure, aiming for the optimum relation between performance and financial matters. In addition, many engineering factors (see Figure 1.2), such as aerodynamics, materials, manufacturing, electrical and mechanical engineering, are involved within the design procedure. Typically, the design objectives are to maximize the energy yield, reduce overall costs and maximize the lifetime of the system. These objectives will determine the minimum cost-of-energy [Ton07].

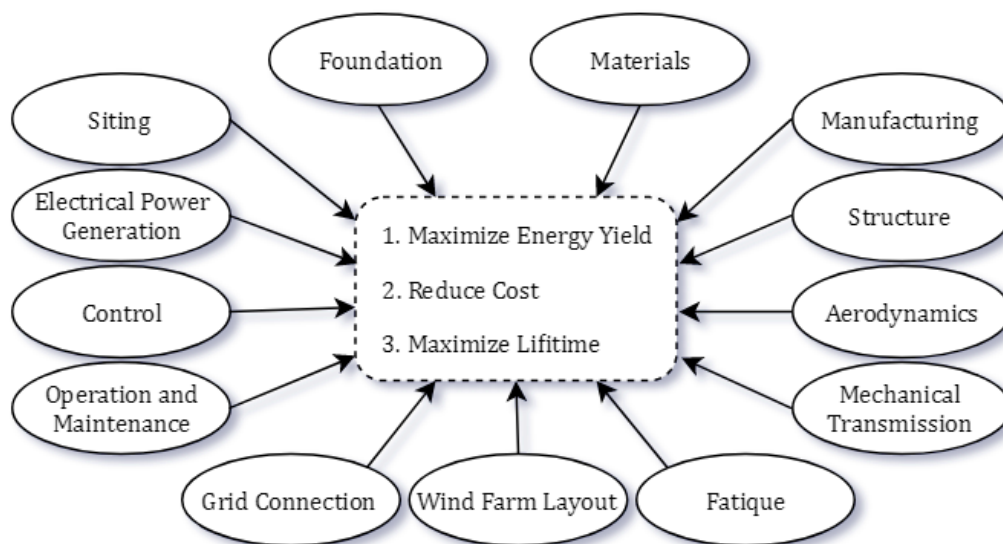


Figure 1.2: Engineering aspects and criteria involved during the design of a wind turbine system.

The first step of a typical design process involves the identification of the subsystems and elements composing the entire wind turbine system. In particular, the most important models for this process are the aerodynamic model, the structural model and the cost model. The aerodynamic model helps in the calculation of the aerodynamic loads, performance and Annual Produced Energy (APE) for a specific rotor configuration and operating conditions, such as ground, weather, region etc. On the other hand, the structural model uses the results from the aerodynamic one and calculates the loads and stresses among the components. Finally, the cost model estimates the manufacturing expenses of the components of the wind turbine system, along with the installation and operating costs. Then, the cost model calculates the Annual Total Cost (ATC).

Based on these models, eventually, the Levelized Cost-of-Energy (LCoE) is computed by dividing the APE by the ATC. Throughout the design optimization, the different variables of the aerodynamic, structure and cost models are altered systematically to yield the minimum LCoE. For the offshore wind turbines, the design process becomes more complicated since there are more costly foundations and tougher operating conditions [Ton07].

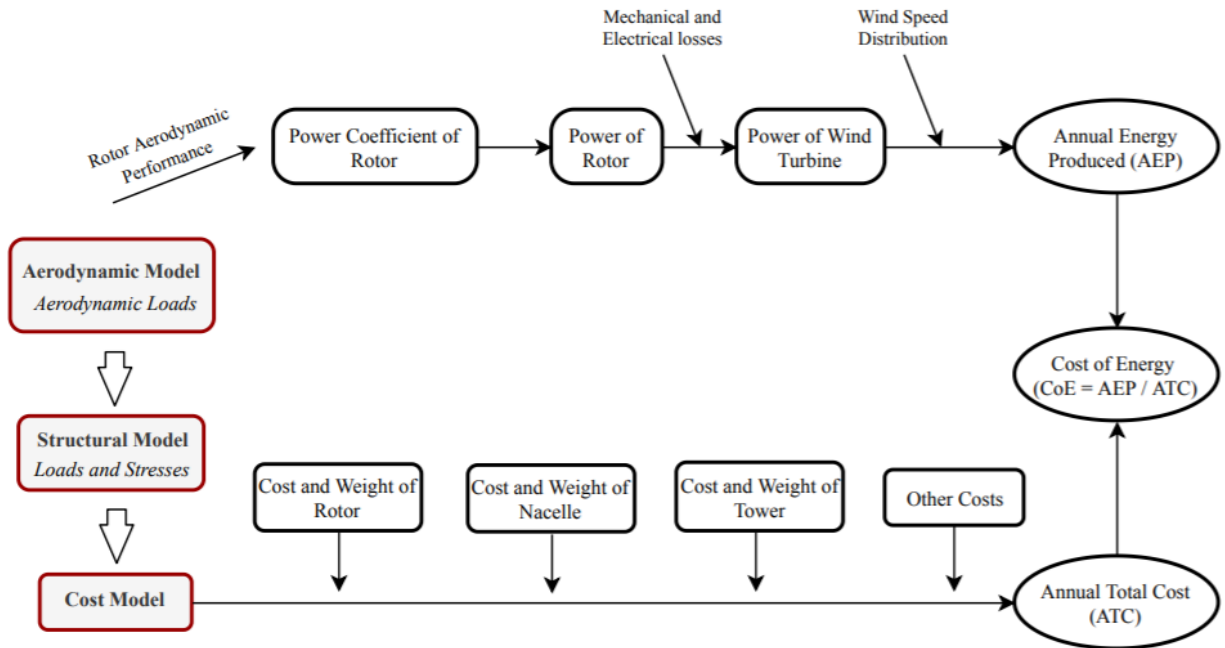


Figure 1.3: Design scheme of a wind turbine.

Aerodynamics contribute significantly in the design process due to the fact that they determine the APE and the aerodynamic loads, which in turn, affect the cost of the different components of the wind turbine system. The aerodynamic design of a wind turbine rotor aims to provide the optimal blade geometry and rotor characteristics that will result in the lowest LCoE, under the three major constraints, which are: the maximization of power coefficient, the maximization of energy yield and the reduction of blade loading. Maximizing the power coefficient is anticipated to increase the energy yield. However, to indeed maximize the energy yield, the power coefficient should be maximized over a wide range of wind speeds. In the earlier days, aerodynamic design focused only on maximizing the power coefficient C_p . Nonetheless, it was discovered that the maximum power coefficient was practically feasible to be achieved only at a small range of wind speeds, especially in stall-regulated turbines with the disadvantage of reducing the annual energy yield [Ton07]. Additionally, increasing the chord and twist of the blades is expected to contribute in increasing the energy yield at low wind speeds as well. This is helpful for sites where the mean annual wind speed tends to be on the low side.

Yet, doing so may increase the blade weight and thus the gravitational loads of the supporting structure [Ton07].

Although deep knowledge of aerodynamics is a prerequisite, it is not enough to identify loads and stresses in elements of the wind turbine. These depend on the deformation of the system components in response to external loads. The aerodynamic loads on the blades act as external loads. The interplay between these aerodynamic loads and the dynamic behavior of the system elements is known as aero-elasticity. In a complex operating environment, the unstable aerodynamic loads have as a coincidence the unstable aerodynamic state of the wind turbine system, which causes great vibrations that reduce the life of the system. Aero-elastic analysis requires aerodynamic models embedded in structural dynamics models. This adds to the computational power required by software design tools [Ton07].

1.3 Principles of Horizontal Axis Wind Turbine Aerodynamics

A horizontal-axis wind turbine (HAWT) is practically consisted of a propeller type rotor and an electrical generator, mounted at the apex of a tower, that extracts kinetic energy from the fluid stream. As the air flows through the rotor, the velocity decreases. Accordingly, the change of the air's momentum will exert an axial force (thrust) on the rotor. Each rotor blade may be considered as a rotating wing, therefore, the airflow around the blades causes the generation of lift and drag forces. These forces yield an output torque at the rotor shaft, resulting in power production. Due to the rotation of the blades, instead of a linear move (as for example in an airplane wing), the local airfoil lift and drag coefficients may be different from those expected from a 2D airfoil analysis. In particular, at high angles of attack, significantly higher values of the aerodynamic coefficients are usually observed due to the phenomenon of stall-delay.

The wake from the rotating blade comprises a vertical shear layer or vortex sheet, as represented in Figure 1.4, which is a schematic reconstruction of the wake formed by a rotating blade, as observed in flow visualization and field measurements. The circulation distribution in the vortex sheet originates from the bound circulation developed at the blades. The former circulation is composed of two vector components:

- **Trailing vortices:** They follow a direction perpendicular to the blade's trailing edge, being related to the variation of the bound circulation.
- **Shed vortices:** They follow a direction parallel to the blade's trailing edge, being related to variation of bound circulation over time.

A HAWT rotor is normally oriented in a way that the axis of rotation is parallel to the incoming wind velocity vector (axial condition). The wake formed behind a HAWT consists of vortex sheets, one per blade, that trace a helical path as a result of rotor rotation. The wake boundary which is usually defined by the radial location of the tip vortices expands downstream as a consequence of the retardation of the flow. The wake vorticity is responsible for slowing down of the air as it flows through the rotor. It will also alter the local angle of attack at the blades, thereby influencing the aerodynamic forces. When the wind speed and rotor speed are constant with time, there is no shed circulation in the wake [Ton07].

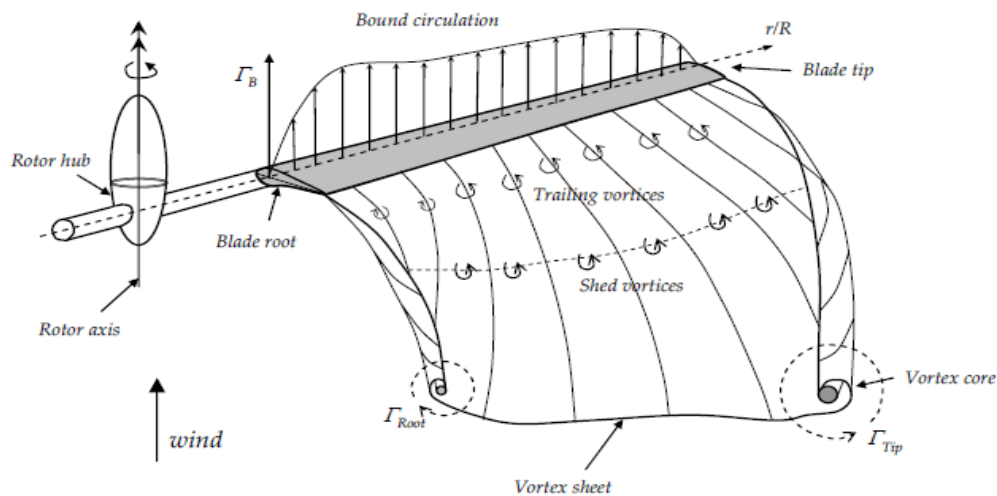


Figure 1.4: Wake developed by a rotating blade of a wind turbine [Ton07].

A yawed rotor operates with its axis of rotation not parallel to the incoming wind velocity vector. In the real operating environment of a HAWT, the direction of the wind changes frequently with respect to the rotor axis. As a result, the turbine may operate in yaw for considerable amounts of time. This yawed condition introduces a cyclic angle of attack at the blades and causes the helical wake to become skewed, yielding an unsteady and complex induction distribution at the rotor plane. In fact, the wake is quite similar to that of a helicopter rotor in forward flight with the main difference being that it expands instead of it contracts. The time-dependent aerodynamic loads at the blades will cause shed circulation in the wake. When the angle of attack at a blade section exceeds the stalling angle of the airfoil, dynamic stall takes place causing the maximum aerodynamic loads to be much higher than those predicted by 2D static airfoil data. The hysteresis effects introduced by dynamic stall may have a negative effect on the aero-elastic damping behavior of wind turbine blades. They reduce the fatigue lifetime leaving an adverse impact on the economics of the system. The flow field across a wind turbine may be separated intuitively into two regions: the global flow field which extends far upstream of the turbine to far downstream and a local (rotor/blade) flow field which is the flow

around the individual blades [Ton07]. Physically these two parts are inherently tied together, but for both the understanding of the physics and also for modeling, it may be convenient to treat them separately. The interaction between the two regions is strong: the flow in the global region determines the inflow condition at the rotor blade and the forces on the blades (which can be seen as a localized pressure change) influences the flow in the global region.

The flow field across a wind turbine may be separated intuitively into two regions: the *global flow field* which extends far upstream of the turbine to far downstream and a *local (rotor/blade) flow field* which is the flow around the individual blades. Physically these two parts are inherently tied together, but for both the understanding of the physics and also for modeling, it may be convenient to treat them separately. The interaction between the two regions is strong: the flow in the global region determines the inflow condition at the rotor blade and the forces on the blades influences the flow in the global region [Ton07].

1.4 The Diffuser-Augmented Wind Turbine

Despite the boom in wind turbine technologies, the unpredictable nature of the wind and its relatively dilute energy content are significant barriers to the wider application of wind turbines; these factors increase the uncertainty on the power output estimations and the cost of energy production. In quest of improving the economics of wind energy harvesting, notable efforts have been made to develop efficient wind concentrators, that is, configurations capable of increasing the energy density of the wind and, thus, enhancing the power output of wind turbines.



Figure 1.5: A Diffuser Augmented Wind Turbine.

The shrouded wind turbine or diffuser augmented wind turbine (DAWT) is considered to be such an innovative wind energy conversion system, that involves the addition of a static diffuser around the rotor (Figure 1.5), in order to control the expansion of the wake and create a region of high

subatmospheric pressure at the diffuser exit. Ultimately, this results in augmenting the mass flow rate passing through the turbine. Therefore, a power performance coefficient beyond the Betz limit is possible to be reached, which means that a DAWT is capable of extracting more power from the wind, compared to a “bare” wind turbine with the same rotor diameter [Lel18].

The basic principle for the energy extraction from the wind implies the existence of a thrust force in the main airflow opposite to the direction of the flow. On a conventional HAWT, the thrust force is obtained because of the rotating blades, which produce a pressure drop across the rotor disk. Accordingly, by increasing the thrust a greater pressure drop could be achieved as well, but contrariwise the airflow through the disk decreases (Figure 1.6). The optimum power coefficient, which is the ratio between the extracted and the available power for a conventional wind turbine is known as the Betz limit and it is equal to $16/27 \sim 0.593$.

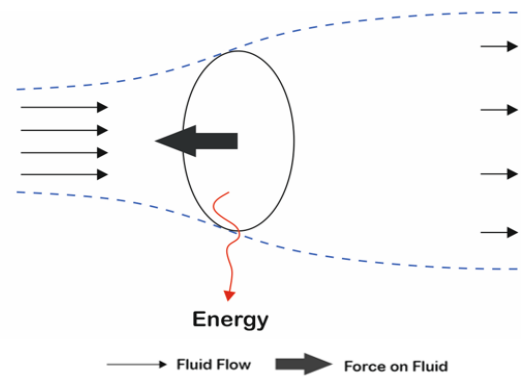


Figure 1.6: Conventional wind energy extraction [Hol11].

The Betz limit could be exceeded, if it is possible to increase the airflow through the rotor disk. The first mechanism to achieve it dictates the exertion of a cross-wind force on the primary mass flow (Figure 1.7), while according to the second one, the increased mass flow is achieved by the mixing of the wake and the external flow behind the rotor, in a lower pressure than the atmospheric (Figure 1.8).

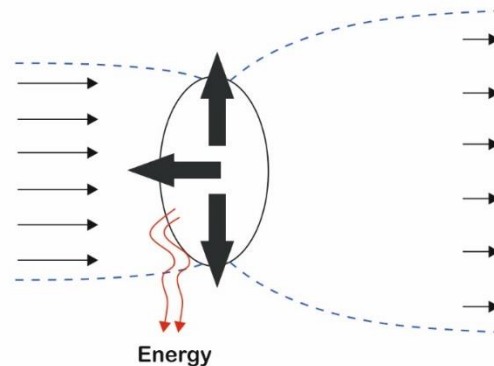


Figure 1.7: Diffuser augmented wind energy extraction [Hol11].

1.4.1 Wind Force Mechanism

Theoretically, when a bare wind turbine operates at the Betz limit, the Momentum (or Actuator Disk) Theory indicates that the wind speed arriving at the rotor plane, will have been decelerated by a factor of $2/3$, compared to the freestream velocity. This particular flow deceleration drives to a pressure rise in front of the rotor, which causes a fraction of the mass flow being pushed sideways around the rotor. By taking into consideration the continuity equation and the incompressible nature of the flow, the rotor, when operates at the Betz limit, captures the energy contained in a stream tube with cross-sectional area equal to the $2/3$ of the rotor's swept area (Figure 1.6) [Lel16].

A mechanism to increase the cross-sectional area of the aforementioned stream tube, is by exerting a force perpendicular to the oncoming wind. This perpendicular force on the primary flow, can be realized by placing an annular lifting device around the rotor with its suction side pointing towards the hub. This annular lifting device can be a shroud or a diffuser formed by an annular wing. From the third law of Newton it is known that the oncoming air stream will try to exert a counteracting force, as shown in Figure 1.8, in order to establish a force equilibrium. This counteracting force can only be exerted by the flow if more air mass is squeezed or sucked through the annular lifting device. So, in effect, this outward force will widen the stream tube, or catchment area, ahead of the rotor as depicted in Figure 1.8 [Lel16].

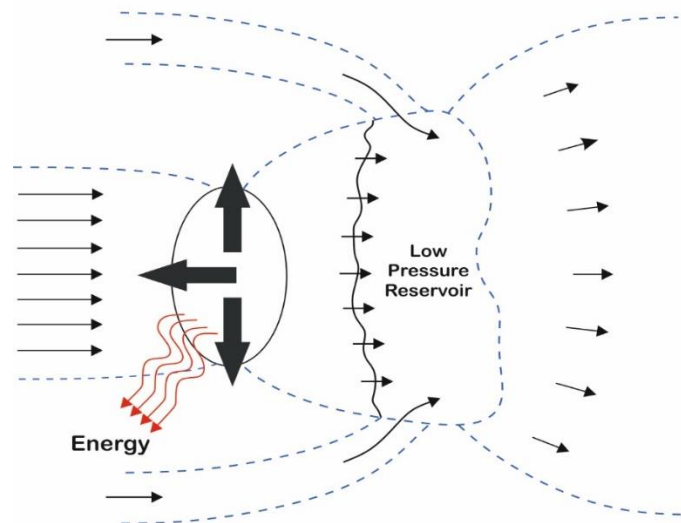


Figure 1.8: Diffuser augmented wind energy extraction scheme, combined with wake and external flow mixing [Hol11].

From a different point of view, the effect of increased mass flow by placing an annular wing around the rotor could also be explained by vortex theory. An annular airfoil, with its suction side pointed towards the center, causes the air flow on the inside surface to accelerate. The suction is related to

the lift of the airfoil and this is again (according to the Kutta-Joukowski theorem) related to the bound vorticity. The annular airfoil generates an inward radial lift force. This lift force is accompanied by a ring vortex, which by the Biot-Savart law will induce a higher velocity on the suction side. In effect, this higher velocity increases the mass flow through the rotor plane. As noted by various scientists, the bound vorticity increases the catchment area in front of the rotor and consequently the “swallowing” capacity of the complete system.

1.4.2 Mixing of the Wake and the External Flow Mechanism

The second power enhancement mechanism makes use of mixing effects. When a rotor extracts energy from an air flow, it will cause, like every other obstacle in a flow, a wake. The wake behind the rotor has a pressure and a velocity deficit as compared to the undisturbed free stream flow. A low pressure behind the rotor is favorable but a low wake velocity is not. As stated by van Bussel [Bus07] and Igra [Igr81], the power augmentation of a DAWT is a direct consequence of the sub-atmospheric pressure around the rotor and exit plane of the shroud. Thus, ideally one wants to maintain a situation behind the rotor where the pressure is low and the mass flow still high. The high mass flow can be established by wake expansion, which is, in fact, already the case with a normal operating wind turbine, or by an increase in wake velocity. The reasoning of the mixing principle is to restore this momentum deficit behind the rotor by mixing the wake flow with the undisturbed free stream flow. The undisturbed free stream flow will in turn provide the extra momentum for the “exhausted” rotor wake flow to recover from the velocity deficit caused by the energy extraction of the rotor. Another reasoning is that the mixing causes the wake to have an additional expansion and thus providing the rotor wake flow with more volume. More wake volume for the same mass flow through the diffuser will result in lower exit pressures behind the rotor and therefore more suction [Lel16].

1.5 Current Status of Aerodynamic Design Models

There is a wide variety of mathematical models that may be used to evaluate the aerodynamic loads on rotors, including the Blade Element Momentum (BEM) method, the Free Wake Vortex method, the Acceleration Potential method and Computational Fluid Dynamics (CFD) techniques [Lel17]. Although the majority of these methods were originally developed to deal with propeller and helicopter rotor aerodynamics, currently they find extensive application within the aerodynamic analysis of wind turbine rotors as well.

The high computational efficiency is the main reason for many aero-elastic design codes to still depend on the Blade Element Momentum (BEM) theory for estimating the aerodynamic loads. The

drawback of this theory is its simplicity and the lack of the physics, necessary to model the complex flow trails around the rotor and may provide unsatisfactory accuracy. Its limitations are mostly observed when treating stalled flows and unsteady conditions such as in rotor yaw. Other methods, such as free-wake vortex methods and CFD, are much more comprehensive; however, they usually require higher computational cost and programming effort in order to be developed.

In the past years, several correction models have been added to BEM theory to improve its accuracy. These mainly took the form of engineering models that mostly fall under airfoil data models that correct 2D static airfoil for 3D effects and inflow models that correct for the uneven induced velocity distribution at the rotor plane due to skewed wake effects in yaw as well as for conditions of heavy and/or unsteady loading on the rotor [Ton07]. It is considered that the increased computer power which will become available to the wind turbine designer, will make it possible to integrate more advanced models in aerodynamic design codes and, moreover, replace BEM-based models thoroughly. This would make research in the field of BEM improvements profitless.

Regarding the present situation, there are numerous reasons why BEM codes should keep being improved. Firstly, the increased computer power that will be used in the future for more complex and advanced aerodynamic modeling will request to use more computational demanding structural analysis codes. Secondly, the accuracy of BEM method is trustworthy when treating low angles of attack conditions in axial flow [Ton07]. In the recent years, it was shown that this method is also sufficiently accurate for stalled conditions provided that reliable airfoil data is used. Last but not least, even though the more complicated methods are inclusive, they do not requisitely give better results than BEM.

1.6 The Structure of the Diploma Thesis

In this Diploma thesis, a Graphical User Interface (GUI) has been developed in order to support a wind turbine analysis software, based on the Blade Element Momentum theory. The particular GUI was entirely implemented using the **C++** programming language, along with **Qt** libraries. The remainder of this Diploma thesis has been organized as follows:

Chapter 2 provides a detailed description on the mathematical formulation of BEM theory, including all the modifications required for the analysis of shrouded rotors as well, and various correction models.

Chapter 3 contains an analytical presentation of the feature of developed GUI.

In **Chapter 4** the ability of the developed software to accurately predict the aerodynamic performance of both HAWT and DAWT rotors is validated against numerical and experimental data.

Finally, in **Chapter 5** the main conclusions of this work are presented.

Chapter 2 – The Blade Element Momentum Theory

2.1 Overview

Blade Element Momentum (BEM) theory is one of the oldest and most widely utilized approaches of lower fidelity for the prediction of wind turbine performance, exploited to substitute the computationally expensive – though higher fidelity – CFD simulations, during the rotor's preliminary design stage. BEM theory is an extension of the actuator disk concept, introduced by Rankine and Froude in the late 19th century, while it was refined and established by Glauert [Gla26], to whom it is attributed. By employing the BEM model, it is possible to estimate the torque and power at the rotor shaft by evaluating the forces acting on the blades, and therefore to determine the optimal geometric characteristics of the rotor (rotor diameter, airfoil profiles, chord, pitch and twist angles), based on the established design criteria.

The method relies on the combination of Blade Element and Momentum theories to estimate the induced axial and tangential velocities on the rotor plane, which in turn define the local flow conditions around the blades and the forces developed on them. Blade Element Theory (BET), assumes that each blade can be divided spanwise into N small elements of length dr , each one located at a radial position r , as illustrated in Figure 2.1. It is assumed that each blade element acts independently of the surrounding ones and operates aerodynamically as a 2D airfoil, whose aerodynamic forces can be calculated based on the local flow conditions. Momentum theory (or Actuator Disk Theory, or Strip Theory) on the other hand, refers to a control volume analysis of the forces acting on the blades, based on the conservation laws of linear and angular momentum.

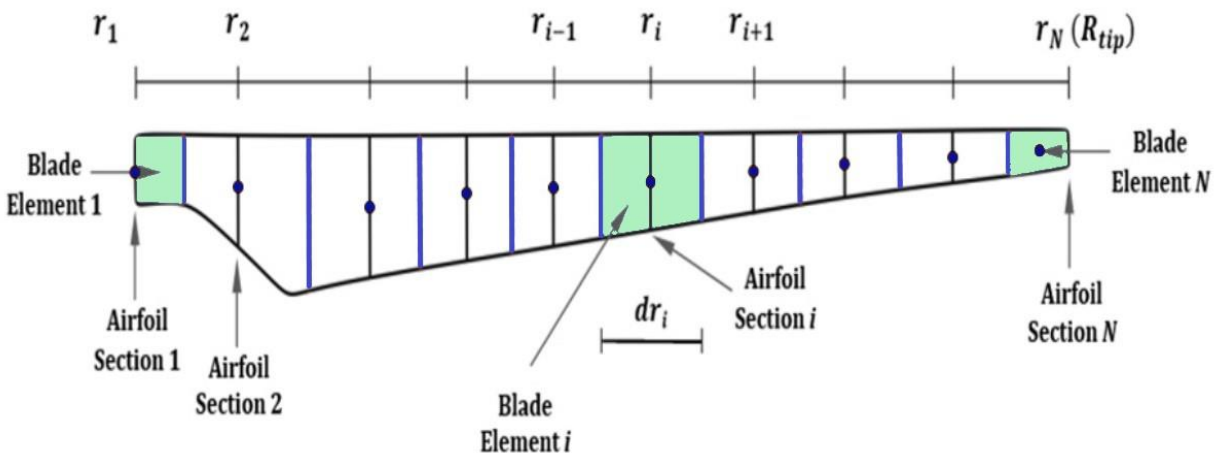


Figure 2.1: Blade elements definition scheme.

To begin with, the streamtube passing through the rotor disk is discretized into N elementary annular streamtubes, as the one presented in Figure 2.2 and Figure 2.3, suchlike the blade. Then for each annular streamtube, it is assumed that the loss of pressure or momentum is caused by the work done by the airflow passing through the rotor plane. In particular, the rate of change of the axial momentum along an annular elementary streamtube starting upstream, passing through the rotor and then moving off into the slipstream, must be equal to the axial force exerted on the corresponding element of the blade, while respectively, the rate of change of the angular momentum of the aforementioned annular streamtube should be equal to the tangential force exerted on the blade element.

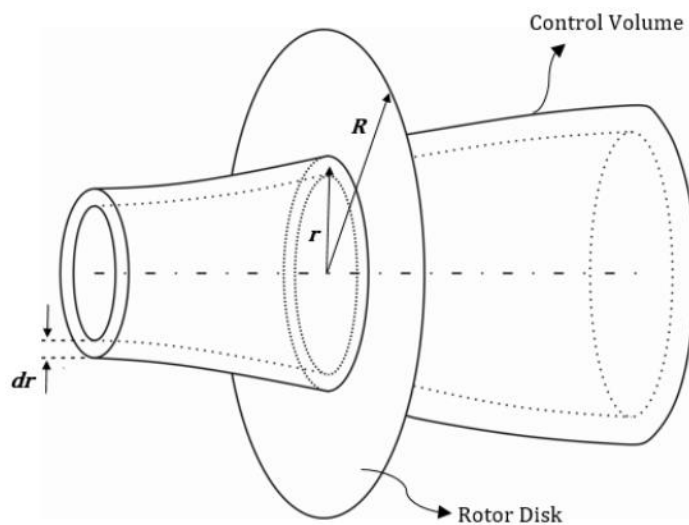


Figure 2.2: An elementary annular streamtube [Han15].

2.2 The 1D Momentum Theory

The mathematical model of 1D Momentum theory presented in this study has been based on the work of Hansen [Han15], aiming to extract the necessary formulas that will be utilized within an iterative procedure for the calculation of the axial and tangential induction factors. At this point, the major assumptions made during the development of 1D Momentum theory, should be highlighted [Han15]:

- *The actual geometry of the rotor is replaced by an ideal actuator disk of negligible thickness.*
- *The velocities and loads are uniformly distributed over the actuator disk.*
- *The flow is considered incompressible and inviscid.*

At first, a control volume, shaped as an elementary annular stream tube, such the one illustrated in Figure 2.2 and Figure 2.3, is considered. The exerted thrust dT , from the air contained in the particular control volume, on the corresponding blade element, according to Newton's 3rd law is equal to the thrust that the blade element exerts on this annular stream tube, and can be found by applying the integral momentum equation, since the cross-section area of the control volume at the rotor plane is $2\pi r dr$ [Lel17]:

$$dT = (V_o - u_1) d\dot{m} = 2\pi r \rho u (V_o - u_1) dr. \quad (2.1)$$

V_o is the velocity of the wind far upstream, u the axial component of the velocity on the rotor plane and u_1 the axial component of the velocity in the wake (Figure 2.3).

The torque dM exerted on the annular stream tube is estimated by applying the integral moment of momentum equation on the control volume, under the assumption that the rotational velocity upstream of the rotor equals to zero. C_θ represents the rotational velocity in the wake [Lel17].

$$dM = r C_\theta d\dot{m} = 2\pi r^2 \rho u C_\theta dr. \quad (2.2)$$

The axial component of the velocity in the wake u_1 , could be expressed by introducing the axial induction factor α_a and the freestream velocity V_o as:

$$u = (1 - \alpha_a)V_o, \quad (2.3)$$

$$u_1 = (1 - 2\alpha_a)V_o. \quad (2.4)$$

The axial (α_a) and tangential (α_t) induction factors are defined respectively as:

$$\alpha_a = \frac{V_o - u}{V_o}, \quad (2.5)$$

$$\alpha_t = \frac{C_\theta}{2\omega r}, \quad (2.6)$$

where ω is the rotational speed of the rotor, measured in rad/s . Therefore, if Eq. (2.3), Eq. (2.4) and Eq. (2.5) are combined with Eq. (2.1) and Eq. (2.2), the thrust and torque exerted from the corresponding blade element on the examined annular stream tube are expressed as follows:

$$dT = 4\pi r \rho V_o^2 \alpha_a (1 - \alpha_a) dr, \quad (2.7)$$

$$dM = 4\pi r^3 \rho V_o \omega (1 - \alpha_a) \alpha_t dr. \quad (2.8)$$

Then, by integrating dT and dM from 0 to R_{tip} , and assuming that the axial induction factor is uniformly distributed over the rotor plane, the total thrust T and torque M exerted on the entire stream tube passing through the rotor disk can be obtained. So, by denoting as A the rotor swept area, the equations providing the thrust (C_T) and power (C_P) coefficients for an ideal bare wind turbine, result as [Lel17]:

$$C_T = T / (0.5 \rho A V_o^2) = 4 \alpha_a (1 - \alpha_a), \quad (2.9)$$

$$C_P = Tu / (0.5 \rho A V_o^3) = 4 \alpha_a (1 - \alpha_a)^2. \quad (2.10)$$

Conclusively, the most significant outcome of the classic 1D momentum theory is that it provides the ability to determine the theoretical maximum power output of an ideal bare wind turbine, by differentiating the power coefficient C_P with respect to the axial induction factor a_a . This results in the well-known Betz limit, which indicates that the maximum energy that an unshrouded wind turbine could extract from the wind, is equal to the 59.3% of the total energy contained in the streamtube passing through the rotor [Bet13].

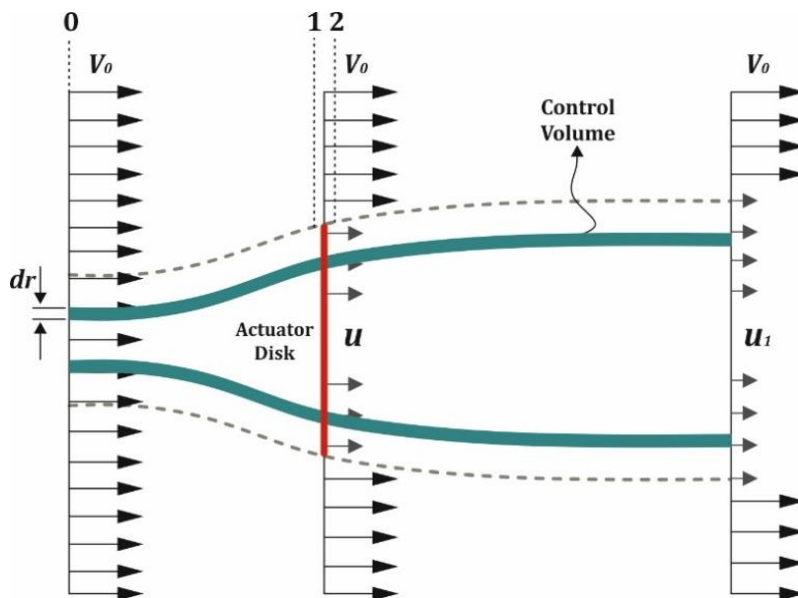


Figure 2.3: The control volume used for the derivation of the 1D momentum theory [Lel17].

2.2 The Classical BEM Model

The Blade Element theory is used to extract alternate expressions for the thrust dT and torque dM developed on each blade element, this time based on the local flow around the blade. It is recalled that each blade element is assumed to operate aerodynamically as a 2D airfoil section [Lel17]. The relative velocity V_{rel} seen by a section of the blade is a combination of the induced axial velocity $(1 - \alpha_a)V_o$ and the induced tangential velocity $(1 + \alpha_t)\omega r$ at the rotor plane, as shown in Figure 2.4. The local angle of attack α is given by:

$$\alpha = \phi - \theta, \tag{2.11}$$

where, θ is the twist angle of the section, i.e. the angle between the chord c and the plane of rotation, and ϕ is the angle between the plane of rotation and the direction of the relative velocity V_{rel} .

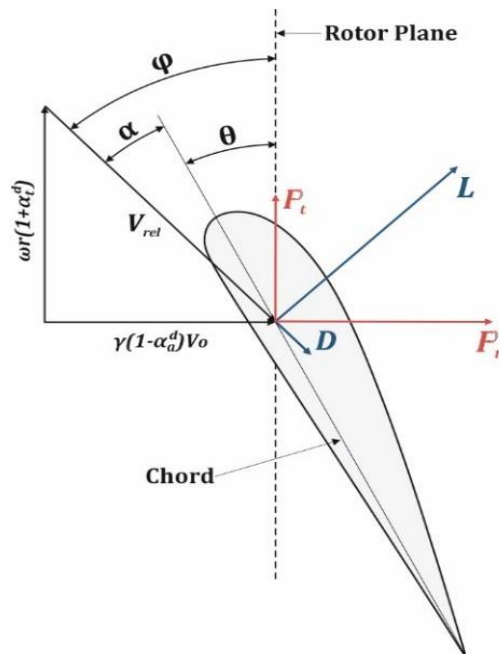


Figure 2.4: Schematic of the induced velocities on the rotor plane [Lel17].

Therefore, the expression connecting the local inflow angle ϕ with the axial and tangential induction factors can be extracted:

$$\phi = \tan^{-1} \left(\frac{(1 - \alpha_a)V_o}{(1 + \alpha_t)\omega r} \right). \tag{2.12}$$

As it is widely known from 2D aerodynamics, the flow past an airfoil section exerts to the airfoil a total aerodynamic force R . Lift is the component of R that is perpendicular to the incoming flow direction, while drag force is the component of R parallel to the flow direction. In this case, the

direction of the incoming flow, is the direction of V_{rel} . Furthermore, if the lift and drag coefficients C_l and C_d are known, the lift L and drag D forces per length can be calculated as [Lel15]:

$$L = \frac{1}{2} \rho V_{rel}^2 c C_l, \quad (2.13)$$

$$D = \frac{1}{2} \rho V_{rel}^2 c C_d. \quad (2.14)$$

In particular, the interest lies only in the forces exerted normal and tangential to the rotor plane. So, by projecting the lift and drag forces into these directions, the normal P_n and tangential P_t forces on the airfoil section are formed as follows [Lel15]:

$$P_n = L \cos\phi + D \sin\phi, \quad (2.15)$$

$$P_t = L \sin\phi - D \cos\phi. \quad (2.16)$$

In addition, Eq. (2.15) and Eq. (2.16) can be expressed in dimensionless formulation, using the normal and tangential force coefficients [Lel15]:

$$C_n = C_l \cos\phi + C_d \sin\phi, \quad (2.17)$$

$$C_t = C_l \sin\phi - C_d \cos\phi. \quad (2.18)$$

where

$$C_n = \frac{P_n}{0.5\rho V_{rel}^2 c}, \quad (2.19)$$

and

$$C_t = \frac{P_t}{0.5\rho V_{rel}^2 c}. \quad (2.20)$$

Conclusively, the thrust and torque on the annular stream tube swept by the examined blade element, given that P_n and P_t are forces per length and denoting the number of the rotor's blades as B , are calculated as follows [Lel15]:

$$dT = B P_n dr, \quad (2.21)$$

$$dM = r B P_t dr. \quad (2.22)$$

Using the following expressions (Eq. (2.23) and Eq. (2.24)), connecting the freestream velocity V_o , the relative velocity V_{rel} , the inflow angle ϕ and the induction factors (α_a and α_t)

$$V_{rel} \sin\phi = V_o (1 - \alpha_a) \quad (2.23)$$

$$V_{rel} \cos\phi = \omega r (1 + \alpha_t) \quad (2.24)$$

along with Eq. (2.19) for P_n and Eq. (2.20) for P_t , then Eq. (2.21) and Eq. (2.22) can be reformed as [Lel15]:

$$dT = 0.5 \rho B \frac{V_o^2 (1 - \alpha_a)^2}{\sin^2 \phi} c C_n dr, \quad (2.25)$$

$$dM = 0.5 \rho B \frac{V_o (1 - \alpha_a) \omega r (1 + \alpha_t)}{\sin\phi \cos\phi} c C_t r dr. \quad (2.26)$$

Ultimately, by equalizing Eq. (2.7) and Eq. (2.25) for dT as well as Eq. (2.8) and Eq.(2.26) for dM , having considered the definition of rotor's solidity $\sigma = Bc/2\pi r$, the expressions for the axial and tangential induction factors, are obtained respectively [Lel15]:

$$\alpha_a = \frac{1}{\frac{4 \sin^2 \phi}{\sigma C_n} + 1} \quad (2.27)$$

$$\alpha_t = \frac{1}{\frac{4 \sin\phi \cos\phi}{\sigma C_t} - 1} \quad (2.28)$$

2.3 The Diffuser Effect on the 1D Momentum Theory

Considering the same assumptions of the classic 1D momentum theory and the elementary control volume shown in Figure 2.4, Rio Vaz [Vaz14] developed a similar formulation to express the modified 1D momentum theory, in which the diffuser effect is also included. The power coefficient of a DAWT is given by [Lel17]:

$$C_p^d = \varepsilon [1 - (V_4/V_0)^2 - (1 - n_d)(1 - \beta^2)\varepsilon^2], \quad (2.29)$$

where, $\varepsilon = V_1/V_0$ is the velocity speed-up ratio, $\beta = A/A_3$ is the reciprocal of the diffuser's exit-area-ratio and n_d is the diffuser efficiency, defined as [Phi03]:

$$n_d = (p_3 - p_2) / [0.5\rho(V_2^2 - V_3^2)]. \quad (2.30)$$

Additionally, applying the energy conservation law between diffuser exit (station 3) and far wake (station 4), as illustrated in Figure 2.4, the axial component of velocity in the wake $V_4 = u_1$ can be provided as [Lel17]:

$$(V_4 / V_0)^2 = \beta^2 \varepsilon^2 + cp_3, \quad (2.31)$$

where, cp_3 is the diffuser exit pressure coefficient, uniformly distributed over the diffuser exit plane [Lel17]:

$$cp_3 = (p_3 - p_0) / (0.5\rho V_0^2). \quad (2.32)$$

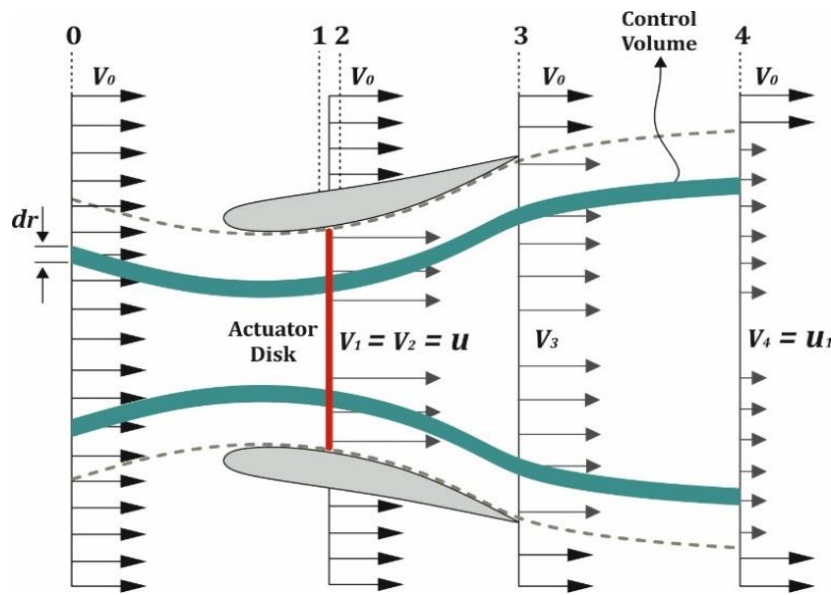


Figure 2.4: The control volume used for the derivation of the diffuser effect on 1D momentum theory [Lel17].

Therefore by combining Eq. (2.31) with Eq. (2.29), the expression that provides the power coefficient can be reformed as [Lel17]:

$$C_p^d = \varepsilon(1 - cp_3) + \varepsilon^3 [n_d(1 - \beta^2) - 1]. \quad (2.33)$$

Earlier, it was explained that the augmentation in power output achieved by a DAWT is imputed to the high sub-atmospheric pressure created at the diffuser exit, which results in an increased velocity and mass flow rate at the rotor plane. A representative velocity distribution along the symmetry axis for an unloaded diffuser configuration (without the presence of a turbine), is shown

in Figure 2.5. The velocity speed-up ratio γ for the unloaded diffuser case is defined as the ratio between the axial velocity of the flow at the rotor plane V_1^d and the freestream velocity V_0 [Lel17]:

$$\gamma = V_1^d / V_0. \quad (2.34)$$

Therefore, the flow velocity at the actuator disk, is given by:

$$V_1 = V_2 = u = (1 - \alpha_\alpha^d)V_1^d = \gamma(1 - \alpha_\alpha^d)V_0. \quad (2.35)$$

The speed-up ratio ε for the DAWT configuration, can be expressed as a function of γ as:

$$\varepsilon = V_1 / V_0 = \gamma(1 - \alpha_\alpha^d), \quad (2.36)$$

where, α_α^d is the axial induction factor for the case of a DAWT.

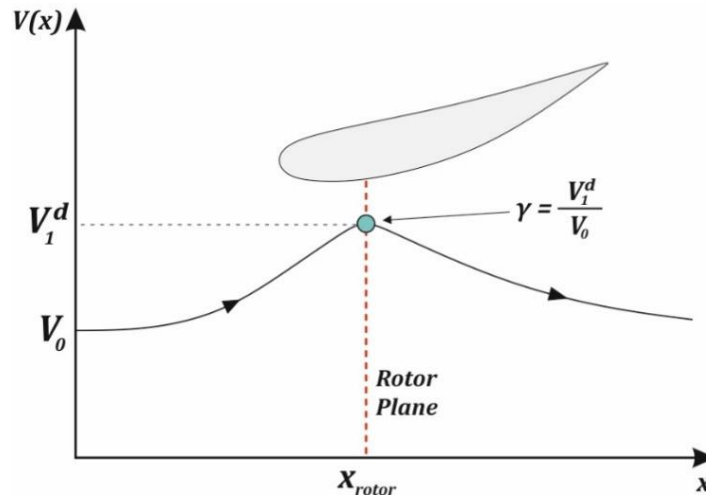


Figure 2.5: The axial velocity distribution along symmetry axis for an unloaded diffuser [Lel17].

Accordingly, by considering Eq. (2.36), which relates ε and γ , Eq. (2.32) and Eq. (2.33) can be reformed as:

$$cp_3 = (1 - \beta^2\gamma^2)(1 - \alpha_\alpha^d)^2 + a_\alpha^d(3\alpha_\alpha^d - 2), \quad (2.37)$$

$$C_p^d = \gamma(1 - \alpha_\alpha^d)^2 [4\alpha_\alpha^d + \gamma^2(1 - \alpha_\alpha^d)(1 - \beta^2)(n_d - 1)]. \quad (2.38)$$

Assuming that the losses through the diffuser are equal to be zero ($n_d = 1$), the thrust and power coefficients can be expressed as functions of the axial induction factor and the velocity speed-up ratio γ as follows [Lel17]:

$$C_T^d = T_d / (0.5 \rho A V_o^2) = 4 \alpha_a^d (1 - \alpha_a^d), \quad (2.39)$$

$$C_P^d = T_d u / (0.5 \rho A V_o^3) = \gamma 4 \alpha_a^d (1 - \alpha_a^d)^2. \quad (2.40)$$

Apparently, if the velocity speed-up equals to 1 ($\gamma = 1$), Eq. (2.40) turns out to be identical to the one obtained by using the momentum analysis for an unshrouded wind turbine (Eq. 2.10), while it should be also mentioned that the power performance coefficient of a DAWT is calculated based on the rotor diameter and not on the diffuser diameter. Nevertheless, a theoretical maximum power coefficient for the DAWT concept cannot be established, as the differentiation of C_P^d with respect to the axial induction factor α_a^d results in a value for the maximum power coefficient equal to $\gamma 16/27$. Thus, the maximum power coefficient is a function of γ , which in turn depends on the geometry of the examined diffuser. Additionally, as Bussel [Bus07] commented, the thrust equation of a DAWT rotor (Eq. 2.39) is similar to the one arising from the analysis of an unshrouded wind turbine; however the reaction of a DAWT system is different, due to the significant impact of the diffuser on the axial induction factor [Lel17].

Eventually, the expressions for the elementary thrust and torque exerted on the examined control volume, according to the modified 1D momentum theory, are highlighted as they will be useful for the modification of the classical BEM theory [Lel17]:

$$dT_d = 4 \rho \pi r dr \alpha_a^d (1 - \alpha_a^d) V_o^2, \quad (2.41)$$

$$dM_d = 2 \rho \alpha_t^d V_1 2 \omega r^2 dA = 2 \pi r^2 \rho V_1 C_\theta^d dr. \quad (2.42)$$

where C_θ^d is the rotational velocity in the wake and $\alpha_t^d = C_\theta^d / (2 \omega r)$ is the tangential induction factor for the DAWT case.

2.4 The Modified Blade Element Momentum Model

Herein, the classical BEM model is reformulated, according to the outcomes of the modified 1D momentum theory that was presented in the previous section, leading to an extended BEM model, which is capable to incorporate the diffuser's effect. According to the modified BEM model, the expression connecting the local inflow angle ϕ with the axial and tangential induction factors is enhanced by the addition of the velocity speed-up ratio γ :

$$\phi = \tan^{-1} \left(\gamma \frac{(1 - \alpha_a^d) V_o}{(1 + \alpha_t^d) \omega r} \right) \quad (2.43)$$

Besides, Eq. (2.23) and Eq. (2.24) are written as:

$$V_{rel} \sin \phi = \gamma V_o (1 - \alpha_a^d) \quad (2.44)$$

$$V_{rel} \cos \phi = \omega r (1 + \alpha_t^d) \quad (2.45)$$

Therefore the equations provide the elementary thrust dT_d and torque dM_d for the case of a DAWT are:

$$dT_d = 0.5 \rho B \frac{\gamma^2 V_o^2 (1 - \alpha_a^d)^2}{\sin^2 \phi} c C_n dr \quad (2.46)$$

and

$$dM_d = 0.5 \rho B \frac{\gamma V_o (1 - \alpha_a^d) \omega r (1 + \alpha_t^d)}{\sin \phi \cos \phi} c C_t r dr. \quad (2.47)$$

Finally, by equalizing Eq. (2.41) and Eq. (2.46) for dT_d as well as Eq. (2.42) and Eq.(2.47) for dM_d , having considered the definition of rotor's solidity $\sigma = Bc/2\pi r$, the expressions for the axial and tangential induction factors for the DAWT case, are obtained respectively [Lel17]:

$$\alpha_a^d = \frac{1}{\frac{4 \sin^2 \phi}{\gamma^2 \sigma C_n} + 1} \quad (2.41)$$

$$\alpha_t^d = \frac{1}{\frac{4 \sin \phi \cos \phi}{\sigma C_t} - 1} \quad (2.42)$$

2.5 Correction Models

Due to the basic assumptions utilized on the mathematical development of BEM theory, it is necessary the numerous correction models to be introduced into the basic BEM scheme, so the computational results to be as similar as possible to the experimental ones. In this part, the major correction models included within the current BEM implementation are presented.

2.5.1 The Prandtl's Correction Model

One of the major limitations of the original BEM theory is that there is no influence of vortices shed from the blade tips into the wake on the induced velocity field. These tip vortices create multiple helical structures in the wake, and play a major role in the induced velocity distribution at the rotor plane. The effect on induced velocity in the rotor plane is most pronounced near the tips of the blades, an area that also has the greatest influence on the power produced by the turbine [Lel15].

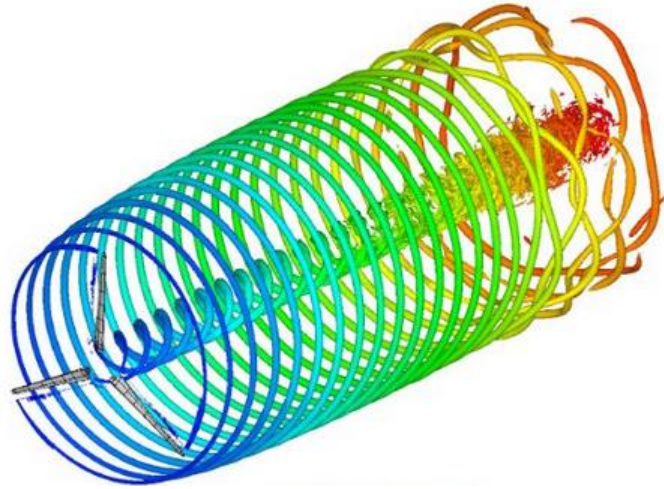


Figure 2.6: Visualization of the tip and hub vortices using CFD simulation.

Prandtl simplified the wake of the turbine by modeling the helical vortex wake pattern as vortex sheets that are convected by the mean flow and have no direct effect on the wake itself. Suchlike, the tip-loss model, the hub-loss model serves to correct the induced velocity resulting from a vortex being shed near the hub of the rotor. The hub-loss model uses a nearly identical implementation of the Prandtl tip-loss model to describe the effect of this vortex. This theory is summarized by a correction factor to the induced velocity field F , which is expressed as follows [Lel15]:

$$F = F_{tip} F_{hub} \quad (2.43)$$

$$F_{tip} = \frac{2}{\pi} \cos^{-1} e^{-f_{tip}} \quad (2.44)$$

$$F_{hub} = \frac{2}{\pi} \cos^{-1} e^{-f_{hub}} \quad (2.45)$$

where

$$f_{tip} = \frac{B (R_{tip} - r)}{2 r \sin \phi} \quad (2.46)$$

$$f_{hub} = \frac{B (r - R_{hub})}{2 r \sin \phi} \quad (2.47)$$

The correction factor F is utilized to adapt the momentum part of the BEM equations, by replacing Eq. (2.7) and Eq. (2.8) with the following ones [Lel15]:

$$dT = 4\pi r \rho V_o 2 \alpha_\alpha (1 - \alpha_\alpha) F dr, \quad (2.48)$$

$$dM = 4\pi r^3 \rho V_o \omega (1 - \alpha_\alpha) \alpha_t F dr. \quad (2.49)$$

Therefore, the expression for the axial and tangential induction factors, including the Prandtl's losses model, are the following [Lel15]:

$$\alpha_\alpha = \frac{1}{\frac{4 F \sin^2 \phi}{\sigma C_n} + 1} \quad (2.50)$$

$$\alpha_t = \frac{1}{\frac{4 F \sin \phi \cos \phi}{\sigma C_t} - 1} \quad (2.51)$$

An identical procedure is also used to extract the expressions providing the axial and tangential induction factors for the case of a DAWT. However, the adoption of a tip-losses correction model during the analysis of a shrouded wind turbine may result in the under-estimation of the power output, since the tip-losses are significantly reduced due to the close proximity of the blades' tips to the internal diffuser wall.

2.5.2 The Glauert's correction model

An additional constraint of the BEM theory appears when the axial induction factor is greater than approximately 0.4 and as a result the 1D momentum theory becomes invalid. The reason for this issue is the wind turbines operating at high tip speed ratios λ , as the rotor enters to the turbulent wake state, where $\alpha_\alpha > 0.5$. According to momentum theory, this operating state occurs when some of the flow in the far wake starts to diffuse upstream, which is a violation of the basic assumptions of BEM theory. This flow reversal cannot practically occur. Flow entrains from outside the wake and the turbulence increases. The flow behind the rotor slows down, but the thrust on the rotor disk continues to increase. Glauert developed an empirical correction to the rotor thrust coefficient C_T

based on experimental measurements of helicopter rotors with large induced velocities. While this model was originally developed as a correction to the thrust coefficient of an entire rotor, it has also been used to correct the local coefficient of the individual blade elements when combined with BEM theory.

In this work, an empirical estimation region is utilized by employing the Glauert's correction model with Buhl's modification [Buh05]. To this end, two non-dimensional parameters are introduced as [Lel17]:

$$k_a = \sigma C_n / (4F \sin^2 \phi), \quad (2.52)$$

$$k_t = \sigma C_t / (4F \sin \phi \cos \phi), \quad (2.53)$$

where F is the Prandtl's hub/tip loss correction factor as calculated in section 2.5.1.

According to Glauert's correction model, different expressions have to be employed for the calculation of the axial induction factor, depending on the utilized estimation region (either momentum theory or empirical expressions), in order to maintain the validity of the momentum theory. Specifically, if $\phi > 0$ and $k \leq 2/3$ the solution falls into the momentum theory region, where [Lel17]:

$$a_a = k_a / (1 + k_a) \quad (2.54)$$

If $\phi > 0$ and $k > 2/3$ the solution falls into the empirical estimation region, and the expression for the calculation of the axial induction factor becomes:

$$a_a = (\gamma_1 - \sqrt{\gamma_2}) / \gamma_3 \quad (2.55)$$

where

$$\gamma_1 = 2Fk_a - (10/9 - F) \quad (2.56)$$

$$\gamma_2 = 2Fk_a - F(4/3 - F) \quad (2.57)$$

$$\gamma_3 = 2Fk_a - (25/9 - 2F) \quad (2.58)$$

Otherwise, if $\phi < 0$ and $k > 1$ the solution falls into the propeller brake region, and the expression for the calculation of the axial induction factor becomes [Lel17]:

$$a_a = k_a / (k_a - 1). \quad (2.59)$$

Finally, if $\phi < 0$ and $k \leq 1$ the value of ϕ cannot possibly be a solution to the BEM equations, therefore a_a should be set to any random value, different from its previous one. The tangential induction factor is given as [Lel17]:

$$a_t = k_t / (1 - k_t). \quad (2.60)$$

During the analysis of a shrouded wind turbine the parameter k_a is given by:

$$k_a = \gamma^2 \sigma C_n / (4F \sin^2 \phi), \quad (2.61)$$

2.5.3 The Shen's correction model

During the implementation of Blade Element Theory, the force exerted on the blade elements near the tip, defined by the 2D airfoil data (lift and drag coefficients), is generally non-zero due to the finite local angle of attack. However, from a physical point of view, the force should tend to zero at the tip, due to pressure equalization, where air is transported from the pressure side to the suction side of the blade. Shen [She05] proposed a correction of the airfoil data near the tip, in order to include 3D tip loss effect within the BEM model. The correction is employed by the introduction of a loss factor F_S , modifying the normal and tangential force coefficients as follows:

$$C_n^{new} = F_S C_n \quad (2.62)$$

$$C_t^{new} = F_S C_t \quad (2.63)$$

The Shen's loss factor F_S is defined as:

$$F_S = F_{S,tip} F_{S,hub} \quad (2.64)$$

where

$$F_{S,tip} = \frac{2}{\pi} \cos^{-1} \left(e^{\left(-g \frac{B(R-r)}{2r \sin \phi} \right)} \right) \quad (2.65)$$

$$F_{S,hub} = \frac{2}{\pi} \cos^{-1} \left(e^{\left(-g \frac{B(r-R_{hub})}{2r \sin \phi} \right)} \right) \quad (2.66)$$

$$g = e^{(-0.125(B\lambda - 21))} + 0.1 \quad (2.67)$$

It is important to note here, while a correction model is included in calculations, only Prandtl's or Shen's losses should be utilized.

2.5.4 Snel's correction for the Himmelskamp Effect

Himmelskamp discovered that the maximum lift coefficient of airfoils on a rotating rotor blade is significantly higher than the maximum lift coefficient of the same airfoil measured on a stationary rotor. The effect is caused by the acceleration of the boundary layer radially due to the centrifugal force, resulting in a thinner boundary layer where the stall is delayed. Furthermore, the air flowing radially, in a rotating reference system, generates a Coriolis force opposite to the rotational direction of the rotor. This force is opposing the rise in pressure of the airfoils suction side and delays the stall even more. This effect is called stall delay or Himmelskamp effect and can be taken into account by modifying the 2D airfoil data. For the affected airfoils the stalled region will shift to higher angles of attack [Mar13]. With a Viscous Inviscid Interaction Method, Snel et al. [Sne95] investigated the flow around a rotating rotor blade and developed a semi-empirical formula to correct 2D airfoil data based on these investigations. According to Snel, only the lift but not the drag coefficient, needs to be modified.

$$C_{l,3D} = C_{l,2D} + \frac{3.1\lambda^2}{1+\lambda^2} \left(\frac{c}{r}\right)^2 \left(\frac{dC_l}{d\alpha}\right)_{lin} (\alpha - \alpha_o) - C_{l,2D}, \quad (2.68)$$

where $\left(\frac{dC_l}{d\alpha}\right)_{lin}$ is the slope of the C_l curve as a function of angle of attack, in the linear region and α_o is the angle in which the lift coefficient is zero.

2.6 The Iterative Scheme

At this point, all necessary equations for the BEM model have been derived and the algorithm for the calculation of the axial and tangential induction factors can be summarized in the following steps. Due to the assumption of no aerodynamic interaction between the elements, each element can be treated separately. Therefore, the application of the BEM algorithm at a specific radius can be computed before solving for another radius while the sequence of in which the elements are treated is irrelevant. For each control volume/blade element, the following algorithm is applied:

Step (1): Initialize α_α and α_t (usually $\alpha_\alpha = \alpha_t = 0$).

Step (2): Compute the local inflow angle ϕ using Eq. (2.12) for a HAWT or Eq. (2.43) for a DAWT.

Step (3): Compute Prandtl's and Shen's correction factors, F and F_S .

Step (4): Compute the local angle of attack α using Eq. (2.11).

Step (5): Compute V_{rel} using Eq. (2.23) for a HAWT or Eq. (2.44) for a DAWT. Then calculate the local Reynolds number.

Step (6): Calculate the lift and drag coefficients (C_l and C_d) for the examined airfoil section at the given flow conditions.

Step (7): Apply Snel's correction to C_l using Eq. (2.68).

Step (8): Compute C_n and C_t from Eq. (2.19) and (2.20).

Step (9): Apply Shen's correction and compute C_n^{new} and C_t^{new} from Eq. (2.62) and (2.63).

Step (10): Calculate α_α and α_t based on the expressions provided by the Glauert correction model.

Step (11): If α_α or α_t has changed more than a certain tolerance ε , go to **Step (2)** or else finish.

Step (12): Compute the local loads on the blade element.

After the completion of the algorithm for each one of the N control volumes/blade elements, the total thrust T and torque M developed on the rotor can be computed by summing up the local loads for each blade element. Therefore, the rotor's thrust and power coefficients, $C_{T,tot}$ and C_P can be formed as follows:

$$C_{T,tot} = \frac{T}{0.5\rho V_o^2 \pi R^2} \quad (2.69)$$

$$C_P = \frac{M\omega}{0.5\rho V_o^3 \pi R^2} \quad (2.70)$$

2.7 The Relaxation Factor

A common problem during the implementation of BEM theory, is the fluctuating behavior of the axial induction factor, as illustrated in Figure 2.7. These fluctuations are caused due to the periodically alteration of the loading state of the rotor disk (C_T value), between light and heavy. Usually, in such situations, after a pre-defined by the user maximum number of iterations, the iteration process stops and the program skips the specific blade element. However, these impacts both the accuracy of the predicted results and the code's performance [Lel15].

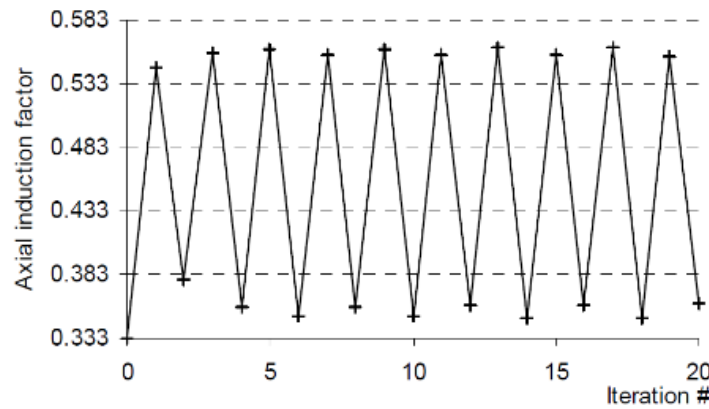


Figure 2.7: Fluctuating behavior of the axial induction factor due to change of loading state [Mah06].

In order to avoid this behavior, Maheri [Mah06] presented a method that employs a relaxation factor ω_{relax} , applicable in the iterative process. The relaxation factor is introduced in the iterations after a new value, a_{k+1} , for the axial induction factor has been calculated [Lel15]:

$$a_{k+1} = \omega_{relax}a_{k+1} + (1 - \omega_{relax})a_k, \quad 0 < \omega_{relax} < 1 \quad (2.71)$$

To further accelerate the convergence rate of the BEMcode, Maheri [Mah06] proposed that for the first few iterations (approximately 10) a relaxation factor $\omega_{relax} = 1$ should be applied, so the first few oscillations to happen. These oscillations will mark the boundaries of the final result's neighborhood. By using a three-point-equation, the axial induction factor is then placed inside this neighborhood [Lel15].

$$a_{k+1} = \frac{1}{4}a_{k+1} + \frac{1}{2}a_k + \frac{1}{4}a_{k-1} \quad (2.72)$$

Then, the iteration proceeds as normal, by applying Eq. (2.71) with the desired relaxation factor.

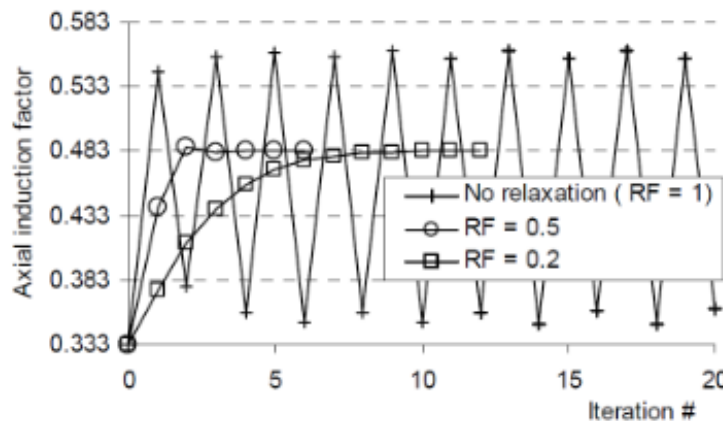


Figure 2.8: Damped fluctuation of the axial induction factor for different relaxation factors. [Mah06].

Chapter 3 – The BEMcode Software

3.1 BEMcode Software Overview

BEMcode is an open-source and user-friendly software, containing all the necessary tools for the BEM analysis of HAWT and DAWT rotors. The GUI of the particular software was entirely developed within this diploma thesis at the School of Production Engineering and Management of Technical University of Crete. In this chapter, **BEMcode** interface is presented, which has been developed using **C++** programming language and **Qt** cross-platform application framework. The code corresponding to the BEM calculations was translated from a previously developed code written in Fortran.

3.1.1 About Qt

Qt is a cross-platform application framework for desktop, embedded and mobile. Supported Platforms include Linux, OS X, Windows, VxWorks, QNX, Android, iOS, BlackBerry, Sailfish OS and others. Qt is *not* a programming language on its own. It is a framework written in C++. A preprocessor, the MOC (Meta-Object Compiler), is used to extend the C++ language with features like signals and slots. Before the compilation step, the MOC parses the source files written in Qt-extended C++ and generates standard compliant C++ sources from them. Thus, the framework itself and applications/libraries using it can be compiled by any standard compliant C++ compiler like Clang, GCC, ICC, MinGW and MSVC.

3.2 Main Window

By launching the program, the application's main window is shown, as depicted in Figure 3.1. Before the creation of a new **BEMcode** project, the main window is composed only by the menu bar, which is a graphical control element containing drop down menus and the status bar. Status bar is a graphical control element that poses an information area, located at the bottom of the main window. At this stage, the menu bar contains only the **File**, **About** and **Help** menus; however, more drop down menus will be added dynamically to the menu bar after the creation of a new project, depending on the user's actions, in order to support the program's functionality.

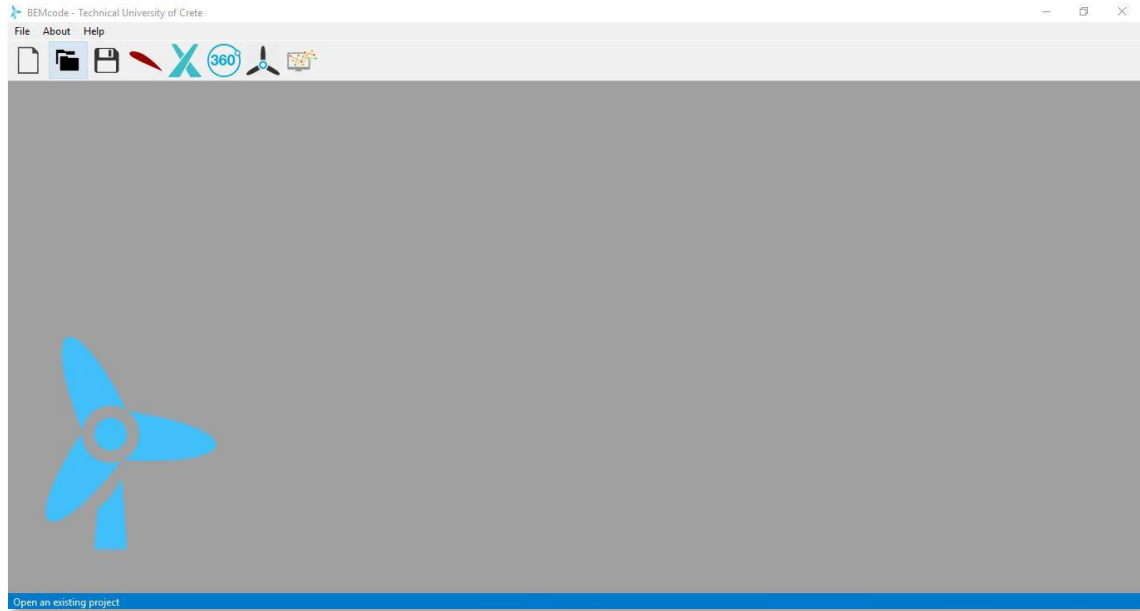
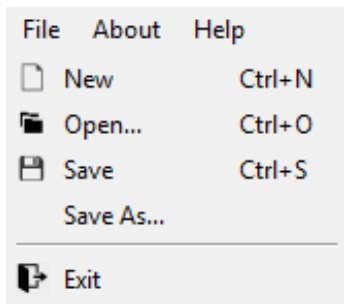


Figure 3.1: Main window of the BEMcode software.

Initial Menus

From the **File** menu, shown in Figure 3.2, the user can choose one of the following actions:



- **New:** Creates a new project.
- **Open:** Opens an existing project.
- **Save:** Saves the current project.
- **Save As:** Saves the current project under a different name.
- **Exit:** Exits the application.

Figure 3.2: The 'File' menu

From the **About** menu, presented in Figure 3.3, the user can find information about the **Qt** toolkit and **BEMcode** software, while from the **Help** menu the user gets access to basic contact information, for any bug reports or questions.

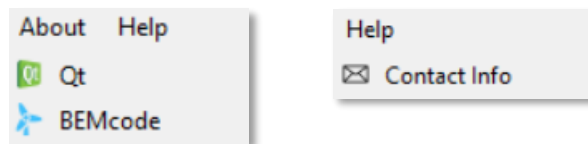


Figure 3.3: The 'About' and 'Help' menus.

Toolbar Menu

The **Toolbar** menu is located below the **Menu** bar and it is consisted of the 3 basic actions contained within the **File** menu as well (*New, Open and Save*), along with the five main modules of the **BEMcode** software. The **Toolbar** menu is shown in Figure 3.4.



Figure 3.4: The Toolbar menu.

The main modules of the software are presented below:

- **Airfoil Dialog:** Opens the Airfoils window and its functions.
- **XFoil Analysis Dialog:** Opens the XFoil analysis window and its functions.
- **360° Extrapolation Dialog:** Opens the 360° Extrapolation window and its functions.
- **Blade Dialog:** Opens the Blade window and its functions.
- **BEM Simulation Dialog:** Opens the BEM simulation window and its functions.



3.3 Airfoil Dialog

In order to create a new project, the user should click the **New** action from the **File** menu. Then, the user is asked to set a name for the new project and define the directory where the project's folder will be created. After the new project has been created, the user can proceed to the **Airfoil Dialog** by clicking the corresponding button from the toolbar menu. The main window is reformed as shown in Figure 3.5; it is composed by a two-axis plot and a 5-column matrix (the rows are added dynamically). Additionally, on the menu bar, an **Airfoil** and a **Plot** menu have been added. In this module the user inserts and manipulates the airfoils composing the rotor blades.

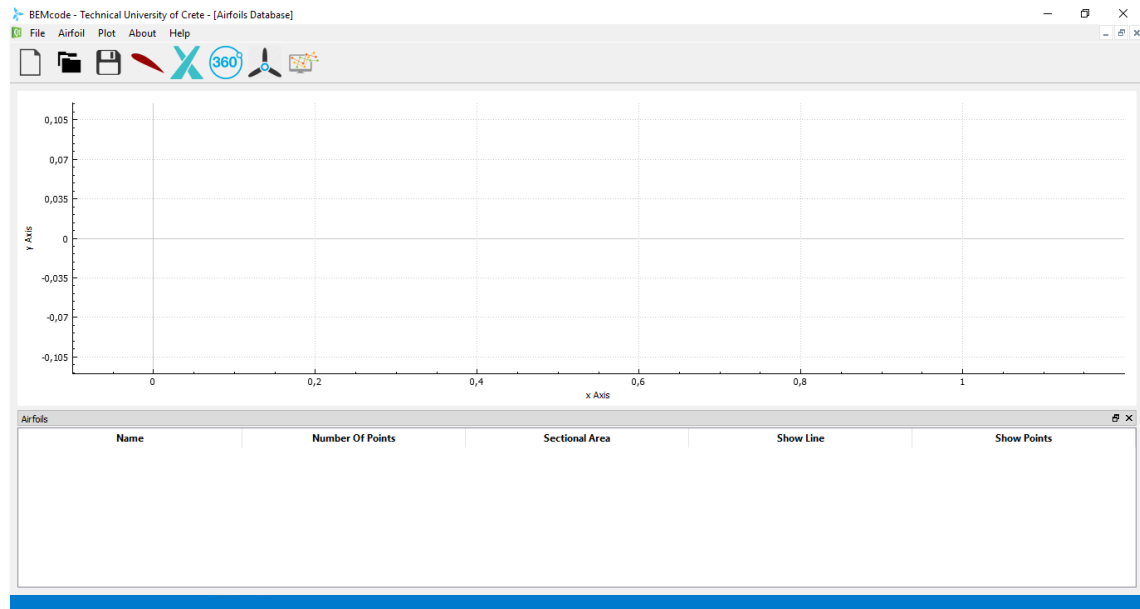


Figure 3.5: The Airfoil main window.

BEMcode provides the following options regarding the generation of a new airfoil geometry:

- *Generation of a standard airfoil geometry from the **NACA** series.*
- *Import an airfoil geometry from the supplied **database**.*

The user can choose one of the above options by clicking on the respective action from the **Airfoil** menu, illustrated in Figure 3.6.

Airfoil Menu

The **Airfoil** menu provides the following functionalities:

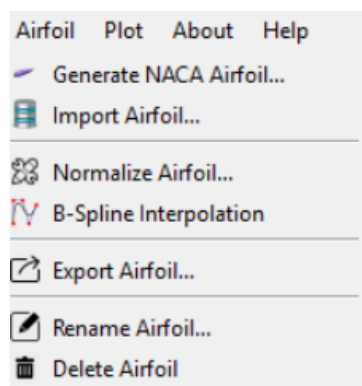


Figure 3.6: The 'Airfoil' menu.

- **Generate NACA Airfoil:** Opens a pop-up window for the creation of a **NACA** airfoil.
- **Import Airfoil:** The user can import an airfoil from the provided database.
- **Normalize Airfoil:** Rescales the airfoil geometry so the chord length to be equal to unity.
- **B-Spline Interpolation:** Interpolates a B-Spline curve through the points of the current airfoil. This feature finds application in cases where the airfoil at hand (usually imported from the database or a different source) is described by a small number of points.
- **Export Airfoil:** Exports the coordinates of a selected airfoil in a **.dat** file format.
- **Rename Airfoil:** Renames the selected airfoil.
- **Delete Airfoil:** Deletes the selected airfoil from the airfoils list.

Plot Menu

By clicking the **Plot** menu, the user has the possibility to do one of the following (Figure 3.7):



Figure 3.7: The 'Plot' menu.

- **Rescale Axes...:** Rescales the axes based on user-prescribed values.
- **Hide All Airfoils:** Hides all the existing airfoils from the plot area.
- **Show All Airfoils:** Shows all the existing airfoils.

Generating a NACA Airfoil

By selecting the option “**Generate NACA Airfoil...**” from the **Airfoil** menu, a new window appears on the screen, as shown in Figure 3.8. On the left side of the particular window a control area exists, in which the user sets the desired parameters for the generation of the NACA airfoil. On the right side, a 2D plot area exists, in which the respective airfoil is displayed.

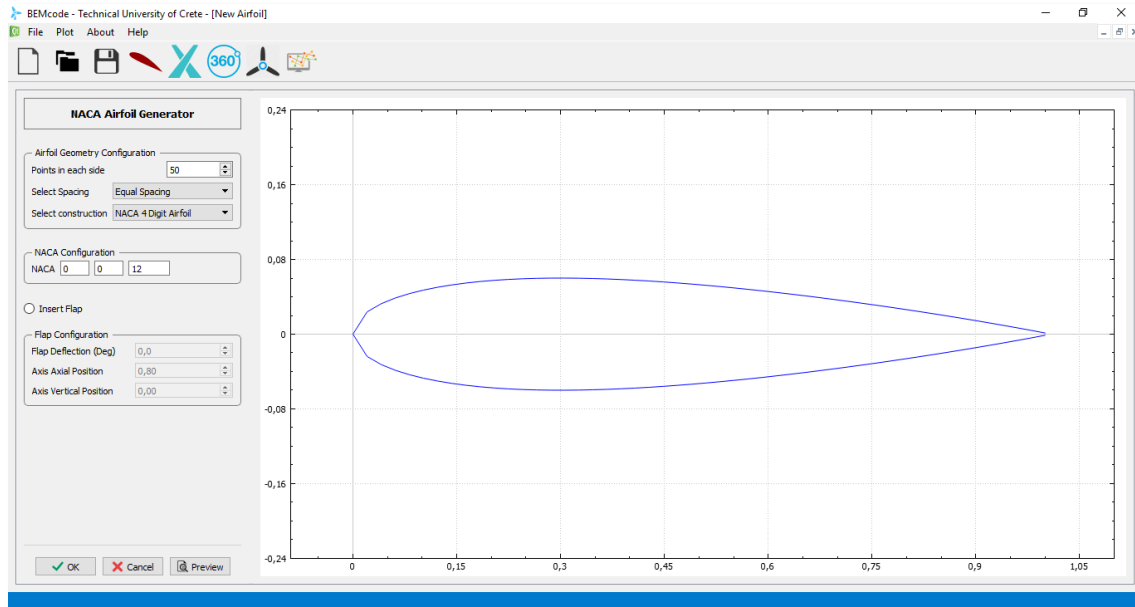
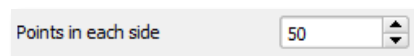


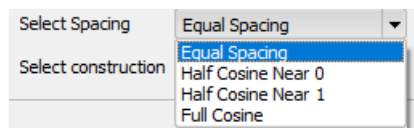
Figure 3.8: NACA Airfoil Generator window.

The **NACA Airfoil Generator** provides the following features:



Points in each side - Spin Box

Defines the number of points in the upper and lower sides of the airfoil.



Select Spacing

Equal Spacing: The points are equally spaced along the chord.

Half Cosine Near 0: The points' distribution is denser at the LE.

Half Cosine Near 1: The points' distribution is denser at the TE.

Full Cosine: The points' distribution is denser at both LE and TE.

Cosine spacing is used to cluster more data points towards the leading and trailing edges of the airfoil, where there are higher curvatures or more detail that needs to be resolved. In Figure 3.9, an example for each one of the spacing options is illustrated.

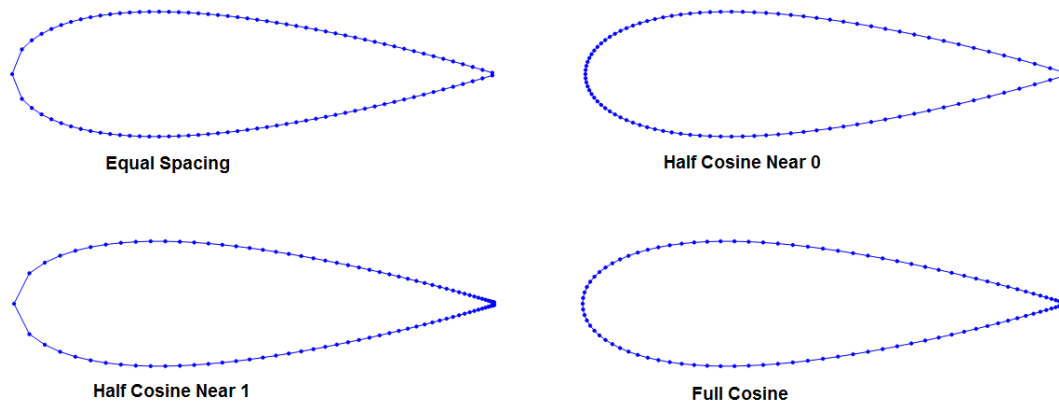
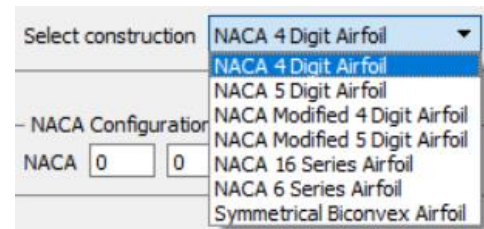


Figure 3.9: An example of the different spacing options, by using the NACA 0012 airfoil as an example.

Select Construction

Determines the type of the NACA airfoil that will be generated. The user is able to choose among the following options:

- *NACA 4-Digit Airfoil*
- *NACA 5-Digit Airfoil*
- *NACA Modified 4-Digit Airfoil*
- *NACA Modified 5-Digit Airfoil*
- *NACA 16 Series Airfoil*
- *NACA 6 Series Airfoil*
- *Symmetrical Biconvex Airfoil*



NACA Configuration

The shape of each NACA airfoil is described by using a series of digits, which are entered into the appropriate NACA equations in order to precisely generate the cross-section of the airfoil. These digits can be provided by the user through the *NACA Configuration field*.

NACA 4-Digit airfoil

First Digit: The maximum camber as a percentage of the chord.

Second Digit: The position of the maximum camber in tenths of the chord.

Last Two Digits: The maximum thickness as a percentage of the chord.

For example, the NACA 0012 airfoil has a camber of 0% located 0% (0.0 chords) from the leading edge with a maximum thickness of 12% of the chord (Figure 3.10).

Figure 3.10: NACA configuration field for a NACA 4-Digit airfoil.

NACA 5-Digit airfoil

First Digit: This digit controls the camber. It indicates the designed coefficient of lift (C_l) multiplied by 3/20.

Second Digit: The position of maximum camber divided by 20.

Third Digit: 0 = normal camber line, 1 = reflex camber line.

Last Two Digits: The maximum thickness as a percentage of the chord.

For example, the first digit of NACA 23012 airfoil is equal to 2, so $C_l = 0.3$, the second digit is equal to 3, so the maximum camber is at the 0.15 or 15% of the chord, third digit is 0, so it has normal camber line and the last two digits are equal to 12, so the maximum thickness is 0.12 or 12% of the chord (Figure 3.11).

Figure 3.11: NACA configuration field for a NACA 5-Digit airfoil.

NACA Modified 4-Digit airfoil

The four first digits stand for the same things as for the NACA 4-Digit airfoils.

Fifth Digit: Indicates the leading-edge radius and is usually one of 0, 3, 6, or 9. 0 indicates sharp leading edge, 3 indicates $\frac{1}{4}$ of the normal radius, 6 is for the normal radius of the 4-digit series and 9 is 3 times the normal radius.

Sixth Digit: The position of the maximum thickness in tenths of the chord.

For the example, the maximum thickness is located at the 40% of the chord (Figure 3.12).

Figure 3.12: NACA configuration field for a NACA modified 4-Digit airfoil.

NACA Modified 5-Digit airfoil

The 5 first digits stand for the same things as for the NACA 5-Digit airfoils and the last two digits for the same as the ones of NACA modified 4-Digit airfoil (Figure 3.13).

NACA Configuration
NACA 2 3 0 12 - 6 4

Figure 3.13: NACA configuration field for a NACA modified 5-Digit airfoil.

NACA 16 Series Airfoil

First Two Digits: It is always 16.

Third Digit: The design lift coefficient (C_l).

Fourth Digits: The maximum thickness as a percentage of the chord.

NACA Configuration
NACA 16 0 12

Figure 3.14: NACA configuration field for a NACA 16 Series airfoil.

NACA 6 Series Airfoil

First Two Digits: The maximum thickness as a percentage of the chord.

Third Digit: The design lift coefficient (CL) multiplied by 10.

Fourth Digits: Mean line chordwise loading effective interval (usually between 0.3 and 0.7).

NACA Configuration
NACA 12 2 0.50

Figure 3.15: NACA configuration field for a NACA 6 Series airfoil.

Symmetrical Biconvex Airfoil

For the construction of a symmetrical biconvex airfoil the user should provide only the maximum thickness as a percentage of the chord.



Figure 3.16: NACA configuration field for a Symmetrical Biconvex airfoil.

Flap Configuration

By enabling the respective radio button, illustrated in Figure 3.17, the user is able to determine the flap's deflection in degrees, as well as the flap's rotation axis axial and vertical positions.

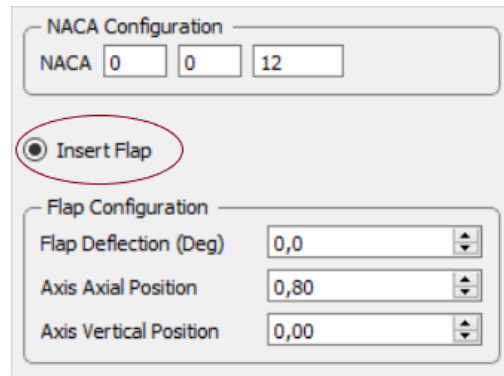


Figure 3.17: Flap insertion enabling.

It is noted that after the commitment of any change in the Airfoil Geometry Configuration, NACA Configuration or Flap Configuration fields, the user should press the **Preview** button in order to update the airfoil plot at the right side of the NACA Airfoil Generator dialog. Then by pressing the **OK** button or the **Cancel** button the user is able to accept or reject the created airfoil geometry respectively.



Figure 3.18: Accept, reject and preview buttons.

For example, assuming that a 5-Digit NACA airfoil is generated and imported to airfoil window (Figure 3.19).

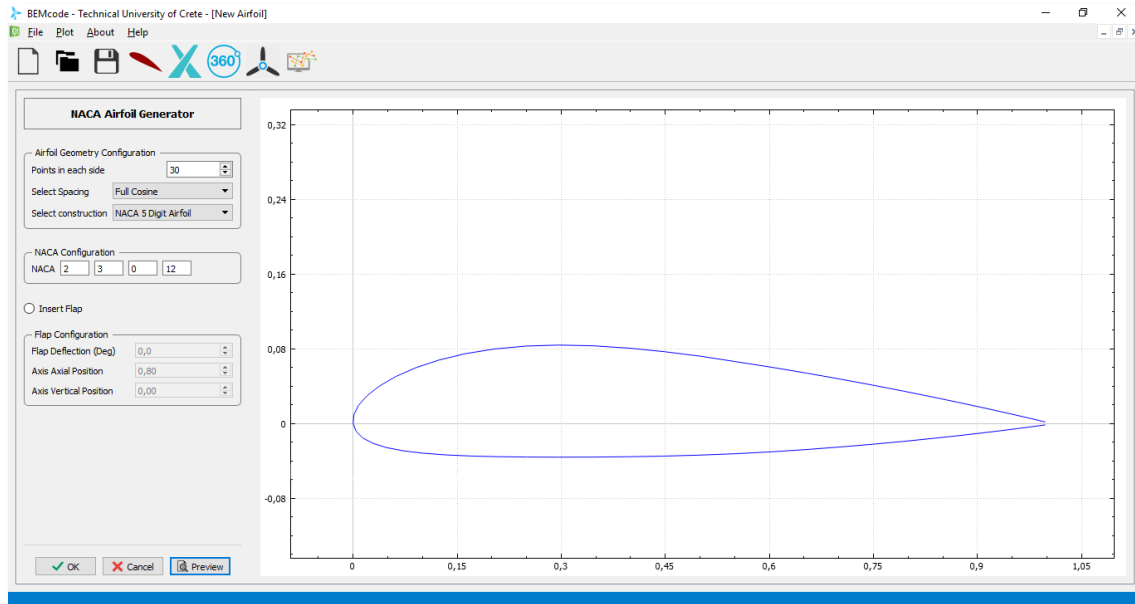


Figure 3.19: A generated NACA 23012.

By selecting the *OK* button, the generated airfoil is loaded to the airfoils list and displayed on the main plot (Figure 3.20). In the “Airfoil Table” a new row is added including information about the airfoil (Name, Number of points and Section area) and the option to hide or show the line and the points of the airfoil.

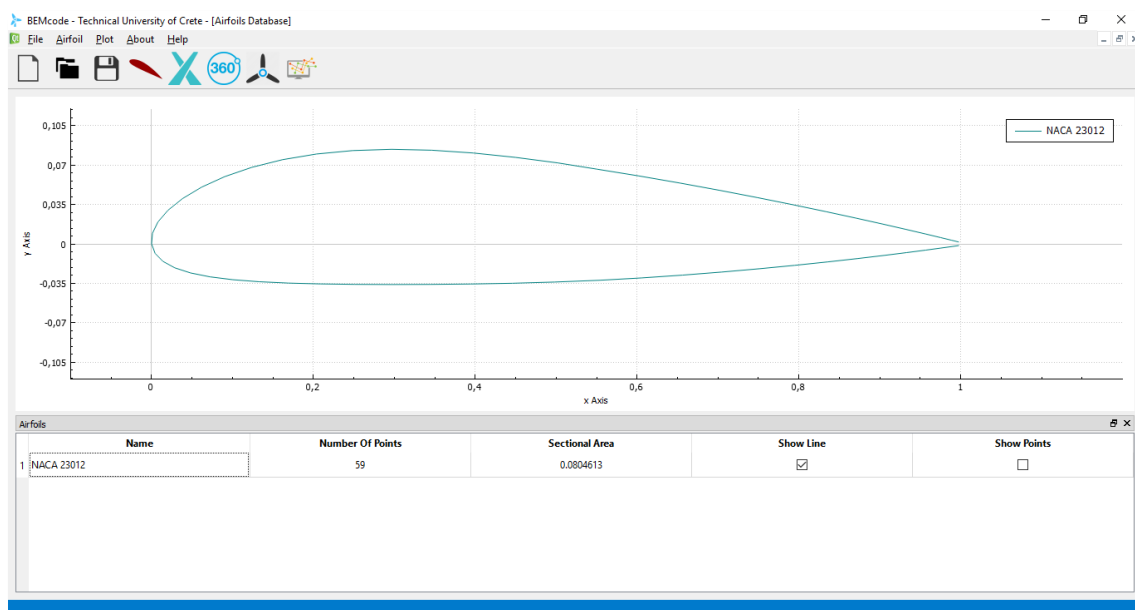


Figure 3.20: A generated NACA 23012 imported to the airfoil dialog.

Moreover, the user, by appropriately use the respective check boxes, is able to hide or show the line or the points of the airfoil (Figures 3.21 & 3.22).

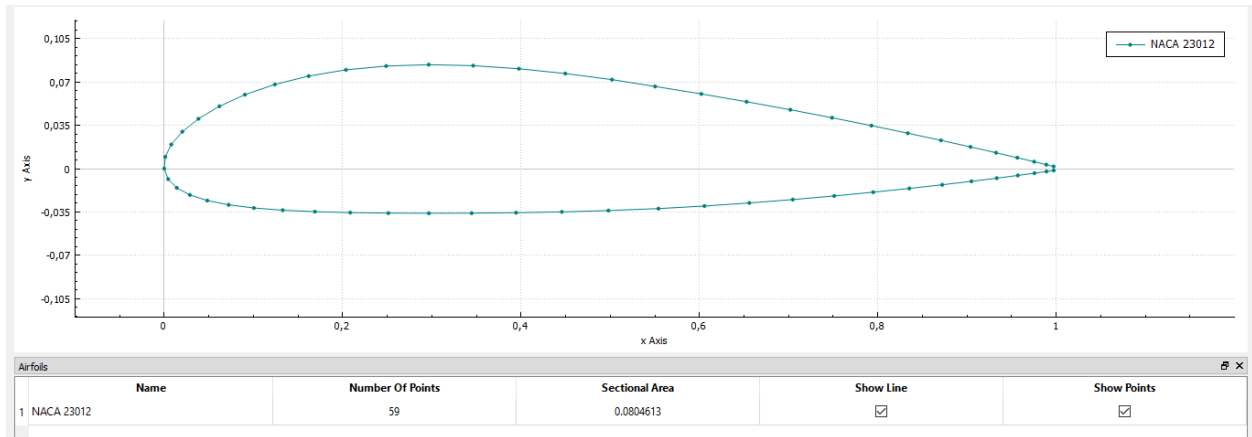


Figure 3.21: Airfoil points shown.

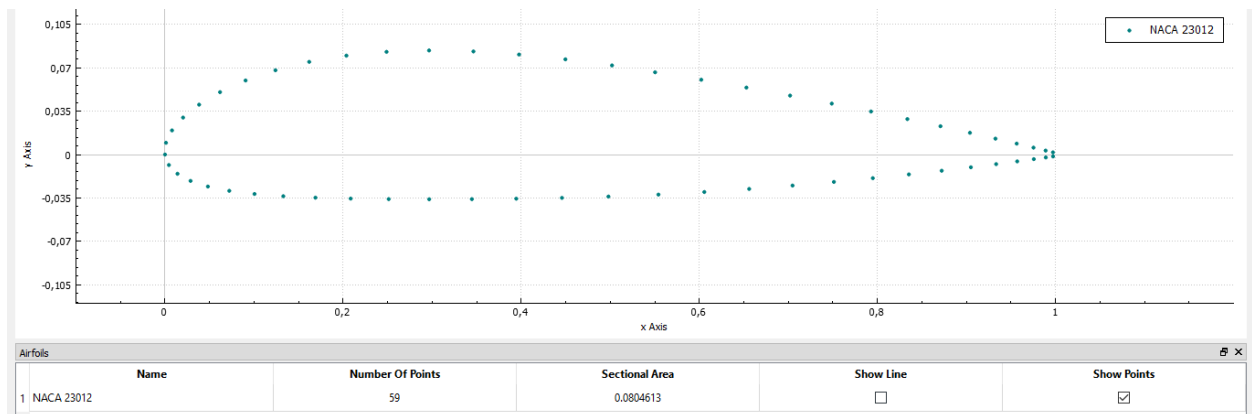


Figure 3.22: Airfoil Line hidden.

Importing an Airfoil

By selecting the option **Import Airfoil...** from the menu, a window including the airfoils database opens (Figure 3.23). The user has a wide selection of airfoils to import in the airfoil dialog.

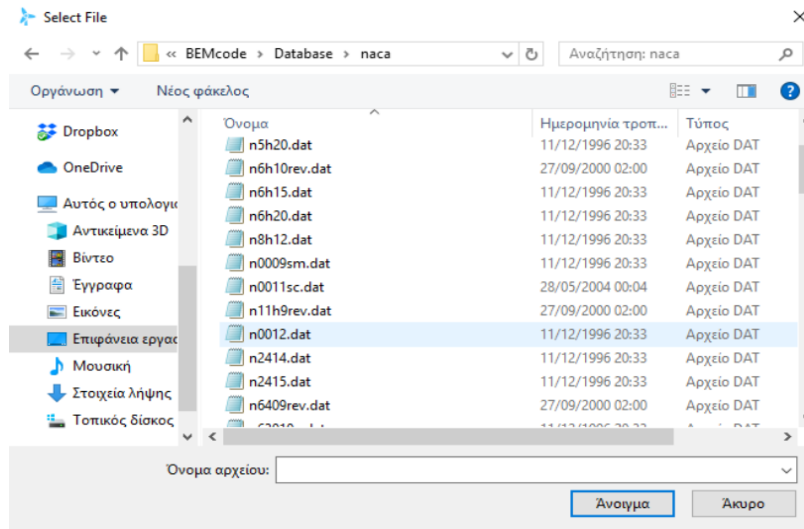


Figure 3.23: Airfoil database window.

Then, the airfoil is imported to the airfoil dialog. All the generated and imported airfoils are visible on the plot (Figure 3.24). The user has the potential to add an infinite number of airfoils.

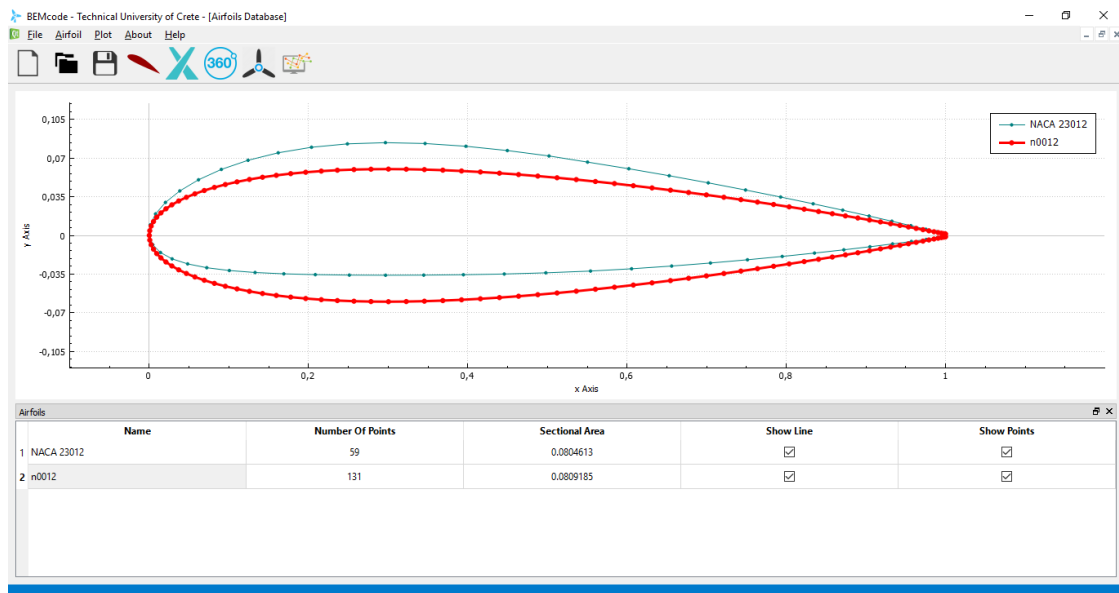


Figure 3.24: Airfoil database window.

3.4 XFOIL Analysis Dialog

The XFOIL code combines a potential flow panel method and an integral boundary layer formulation for the analysis of the flow around airfoils (no computational mesh is required). Given the coordinates specifying the shape of a 2D airfoil, Reynolds and Mach numbers, XFOIL can calculate the pressure distribution on the airfoil and hence lift and drag characteristics at a given angle of attack. The code was developed to rapidly predict the airfoil performance at low Reynolds numbers and its convergence is achieved through the iteration between the outer and inner flow solutions on the boundary-layer displacement thickness. Thus, the XFOIL code calculates the viscous pressure distribution and captures the influence of limited trailing-edge separation and laminar separation bubbles. The XFOIL code tracks only the most amplified frequency at a given point on the airfoil downstream from the point of instability to obtain the amplitude of that disturbance.

In order the *XFOIL* dialog to operate properly, the user has to add airfoils in the *Airfoil* dialog. The main window of the XFOIL dialog is splitted in two parts as shown in Figure 3.25. *XFOIL Analysis* data are included in the left part of the window and the right part is composed of a 2D plot.

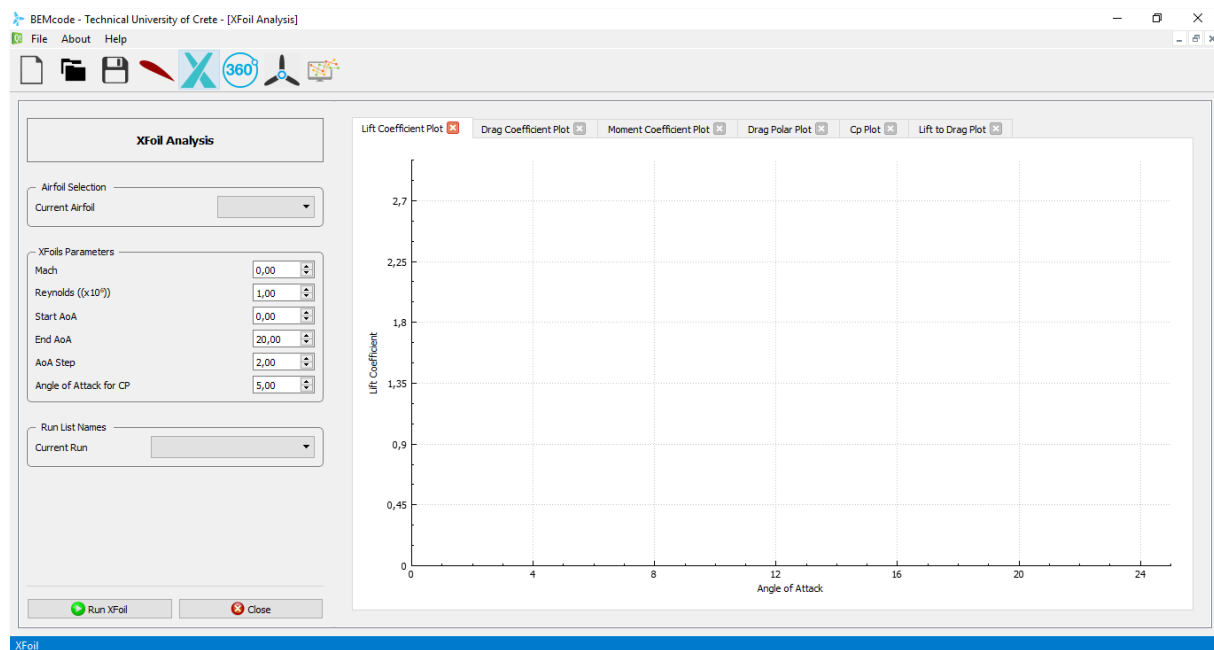


Figure 3.25: Xfoil Analysis window.

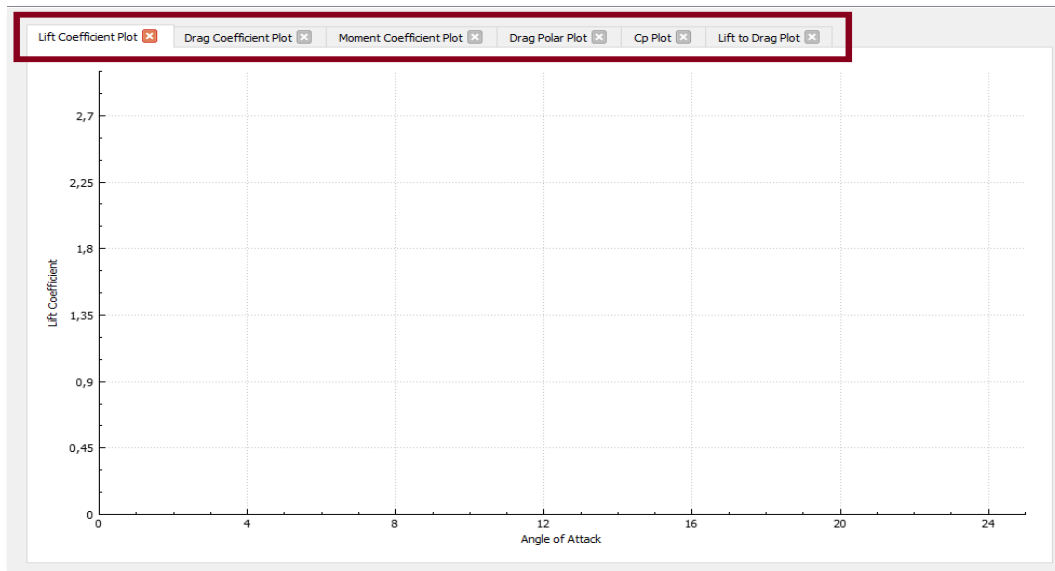


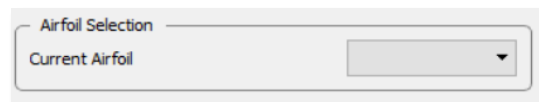
Figure 3.26: XFOIL Tabs - Plots.

In the upper side of the plot in this dialog, there are 6 tabs, on each of them, after the XFOIL analysis iterations terminate, 2D graphs are resulted. The lift, drag, and moment coefficients (C_l , C_d , C_m), drag polar, the pressure coefficient distribution (C_p) around the airfoil (for the pre-set angle of attack), as well as lift to drag ratio at each angle of attack are plotted in the main window (Figure 3.26).

The XFOIL Analysis provides the following features:

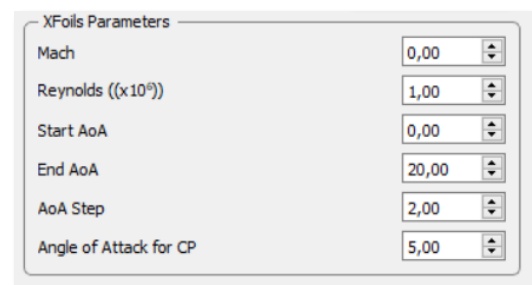
Airfoil Selection – Current Airfoil

A combo box that includes the airfoils which exist in the Airfoil window. The selected airfoil will be analyzed when the Run XFOIL button is pressed.



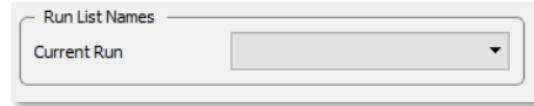
XFOIL Parameters

- Mach: the Mach number.
- Reynolds: the Reynolds number.
- Start AoA: The lowest angle of attack that will be examined (degrees).
- End AoA: The highest angle of attack that will be examined (degrees).
- AoA Step: The angle of attack increment step (degrees).
- Angle of attack for Cp: the angle of attack for which the pressure coefficient will be printed.



Run List Names

A combo box that holds the names of the Runs that have been done.



It is noted that after selecting an airfoil from the Airfoil Selection Box and the commitment of any change in the XFOIL Parameters, the user, by pressing the **Run XFOIL** button or the **Close** button is able to start the XFOIL analysis or close the XFOIL dialog (Figure 3.27).



Figure 3.27: XFOIL buttons.

Running XFOIL Calculations

If the user presses the Run XFOIL button for a selected airfoil, the XFOIL solver runs in the background (Figure 3.28) and subsequently, the results are plotted on each tab. When the XFOIL calculations are finished, the name of each “Run” is appeared in the Run List Names Combo-box (Figure 3.29). The user has to run the XFOIL calculations for each airfoil in order its results to be plotted.

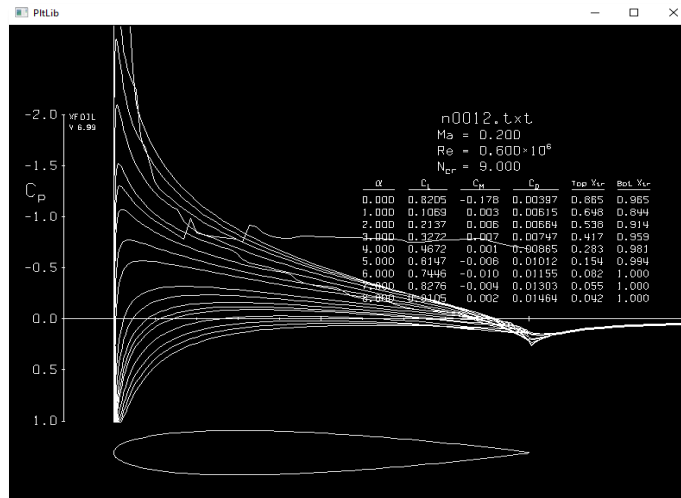


Figure 3.28: XFOIL script.

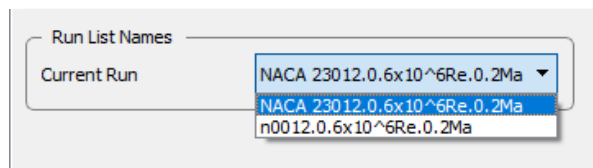


Figure 3.29: Run List Names Combo-box after the XFOIL calculations.

Tabs - Plots

Assuming that the airfoils of the previous section (3.3), NACA 23012 and NACA 0012, are considered as an example as well for this one, the resulted plots are:

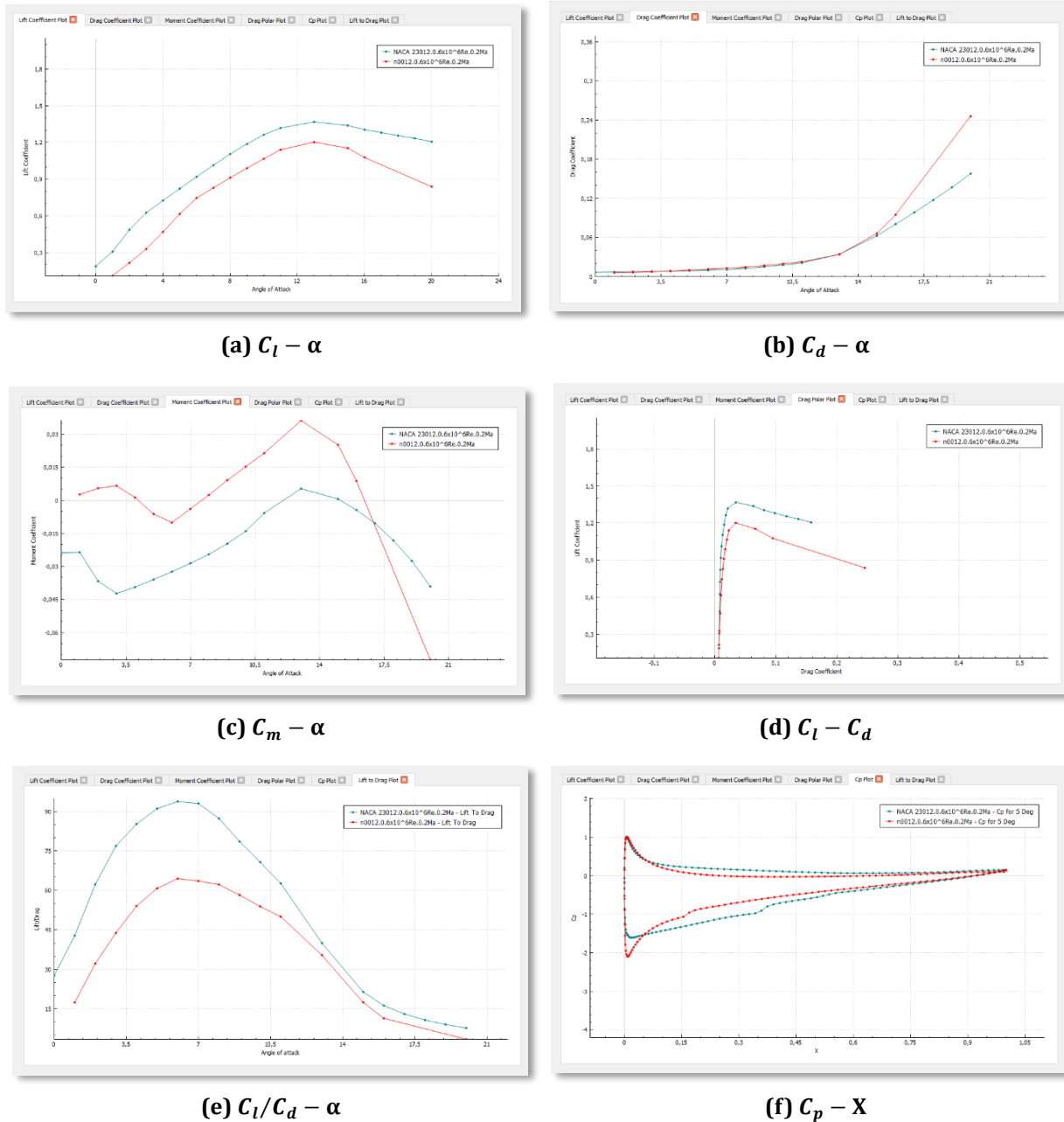


Figure 3.30: XFOIL resulted plots.

Edit Menu

By the time the first run has been completed, a new menu selection appears on the **Menu** bar in the **XFOIL** window (Figure 3.31).

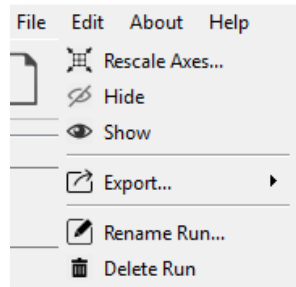


Figure 3.31: "Edit" menu.

Selecting the *Edit* menu, the user can choose one of the following options:

- **Rescale Axes...:** Rescales the axes of a selected plot based on user-prescribed values (Figure 3.32 & 3.33).
- **Hide:** Hides the graph of the selected run.
- **Show:** Shows the graph of the selected run.
- **Export...:** Exports the results of a selected run and plot in **.dat** file format (Figure 3.34).
- **Rename Run...:** Renames a selected run (Figure 3.36).
- **Delete Run:** Deletes a selected run.

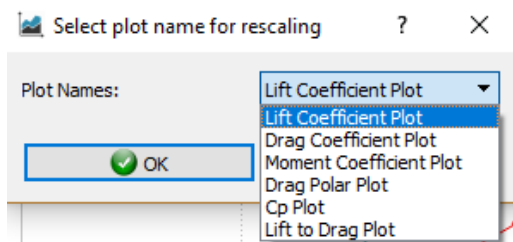


Figure 3.32: Plot selection for rescaling.

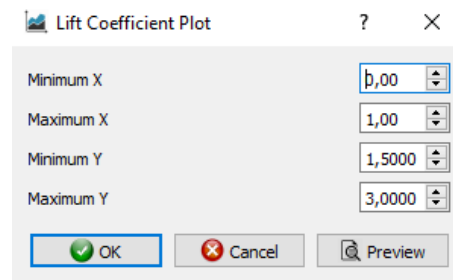


Figure 3.33: Rescaling input box.

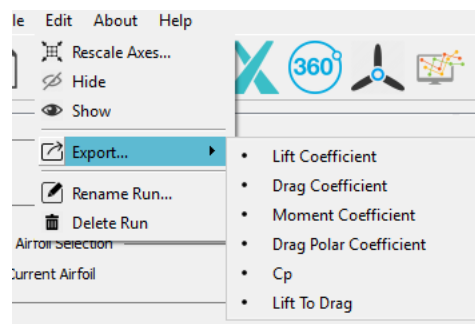


Figure 3.34: Plot List for exportation.

For example, if the user selects the “Drag Coefficient” option for the NACA 0012 airfoil, Mach number equals to 0.2 and Reynolds number equals to 0.6×10^6 , then the .dat file format will have the name **n0012.0.6x10⁶Re.0.2Ma.dat** and will include the values of the drag coefficient at each angle of attack (Figure 3.35).

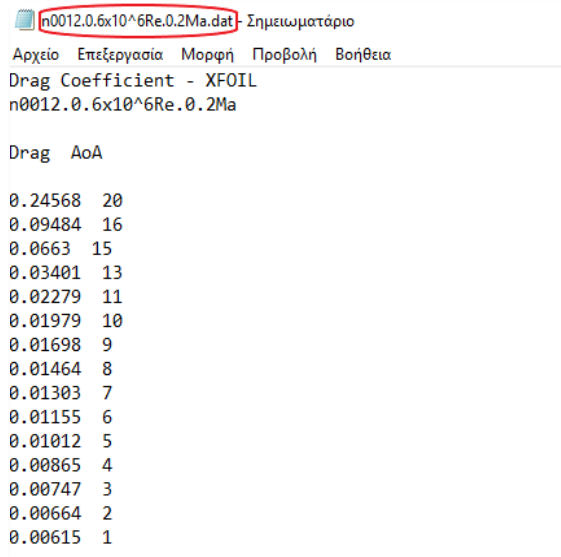


Figure 3.35: XFOil exported data .dat file.

By clicking the *Rename* option from the *Edit* menu, the user is able to change the name of the selected run.

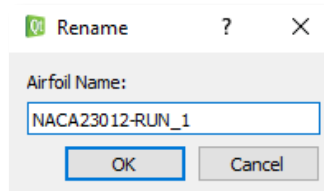


Figure 3.36: Rename pop-up box.

As the user presses the OK button, the previous name of the selected run is replaced by the new one (Figure 3.37).

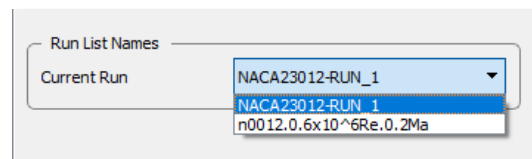


Figure 3.37: The updated Run List Names.

3.5 360° Extrapolation Dialog

During the simulation of wind turbine applications, especially when low tip-speed ratios are examined, the angle of attack in certain regions of the rotor blades can be as high as $60^\circ - 70^\circ$. Additionally, such high angles of attack should also be encountered when studying stall regulated wind turbines, where deep stall is invited, in order to limit the excessive power in high winds. Therefore, during the implementation of the BEM algorithm, aerodynamic coefficients at any angle of attack may be required. However, XFOIL is capable to estimate lift and drag coefficients for airfoils functioning to angles of attack that lie before and just beyond stall, i.e. approximately between -10° and 30° . In order to overcome this shortcoming, the lift and drag coefficients tables have to be extrapolated to the full 360° range.

The user enters the 360° Extrapolation dialog by pressing the button on the toolbar menu (Figure 3.38). In order this dialog to operate properly, the user has to complete at least one “run” in the XFOil window. On the upper side of the plot in this dialog, there are 2 tabs, the lift and drag coefficient plot, in which results can be plotted when the user selects one name from the *Run List Names*.

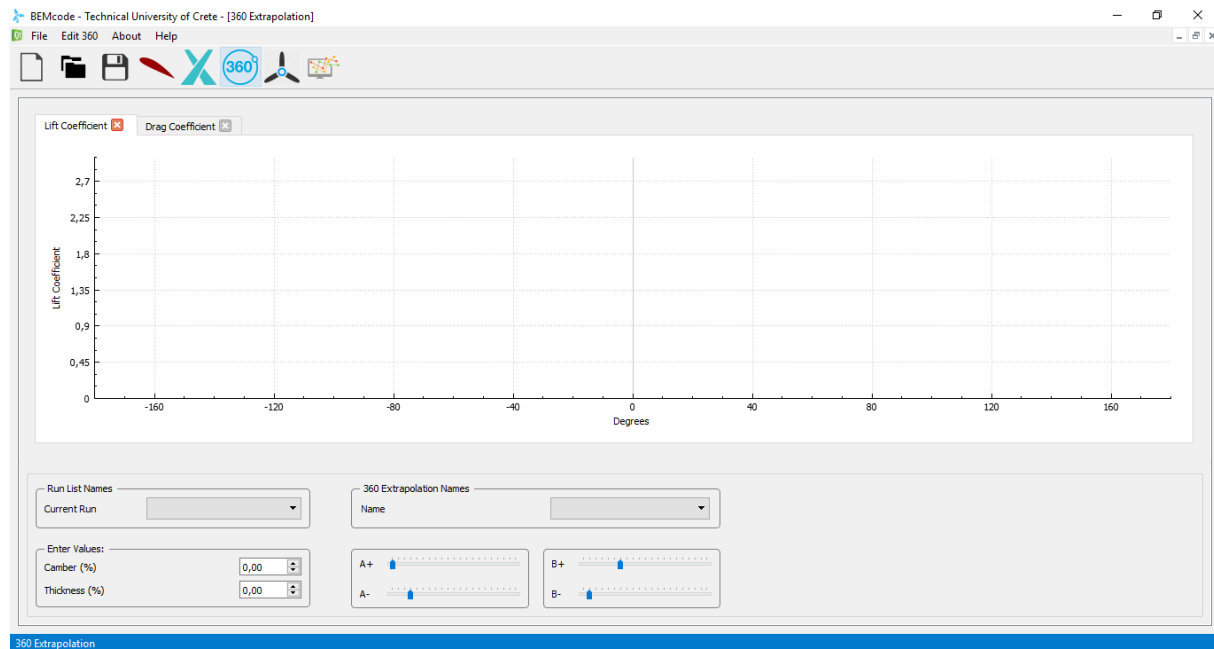
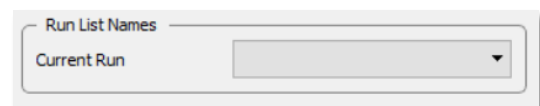


Figure 3.38: 360° Extrapolation main window.

On the lower side of the 360° Extrapolation main window there are the following features:

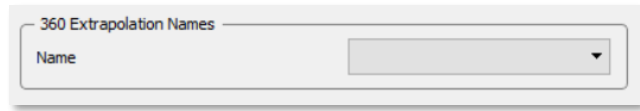
Run List Names:

A combo box that holds the names of the Runs that have been done.



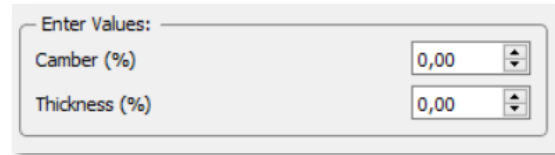
360 Extrapolation Names:

A combo box that holds the names of the 360° extrapolations that have been done.



Parameters:

- Camber (%): The Camber number (%).
- Thickness (%): The thickness number (%).



Graphs Curvature Slide-Bar

Slide-bars allow user to re-form the curve on the lift and drag coefficient plot.



Edit 360 Menu

A new menu selection - the **Edit 360** menu - appears on the Menu bar in 360° Extrapolation main window (Figure 3.39).

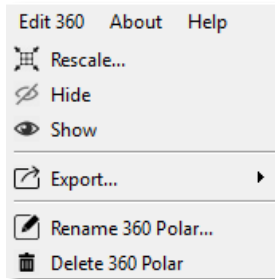


Figure 3.39: The Edit 360 menu.

Selecting the *Edit 360* menu, the user can choose one of the following options:

- **Rescale...:** Rescales the axes based on user-prescribed values.
- **Hide:** Hides the graph of the selected 360° Extrapolation run name.
- **Show:** Shows the graph of the selected 360° Extrapolation run name.
- **Export...:** Exports the results of a selected run and plot in **.dat** file format.
- **Rename 360 Polar...:** Renames a selected 360° Extrapolation run name.

- **Delete 360 Polar:** Deletes a selected 360° Extrapolation run name.

Lift & Drag Coefficient Plots

The Run List Names combo-box is filled automatically with data taken from the XFOIL window. As an example, it will be used a NACA 0012 airfoil, imported in Airfoil window and analyzed in XFOIL window (Figure 3.40).

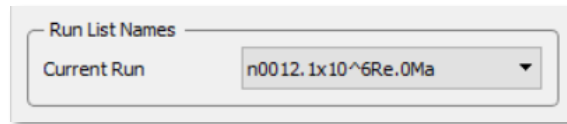


Figure 3.40: Example airfoil selection.

When the user selects the name from the Run List Name combo-box, then a “Method Selection” pop-up box appears (Figure 3.41). The user defines the method that will be used in order the 360° extrapolation to be exceeded. The options are the Montgomerie’s method, the Viterna’s method or the data to be imported from QBlade. Once the user selects one method, the mathematical calculations for the extrapolation run in the background. As a result, the *Lift* and *Drag Coefficient* plots are displayed in the main window (Figure 3.42 & 3.43).

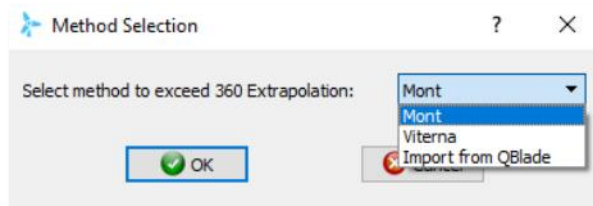


Figure 3.41: The 360° Extrapolation Method selection box.

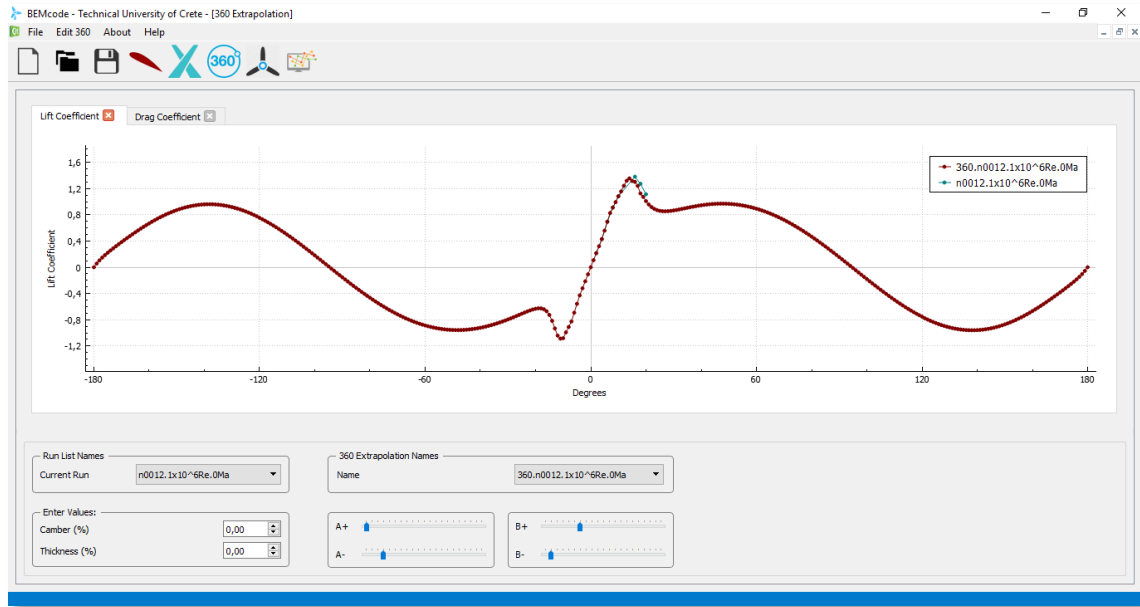


Figure 3.42: The 360° Extrapolation Lift Coefficient plot.

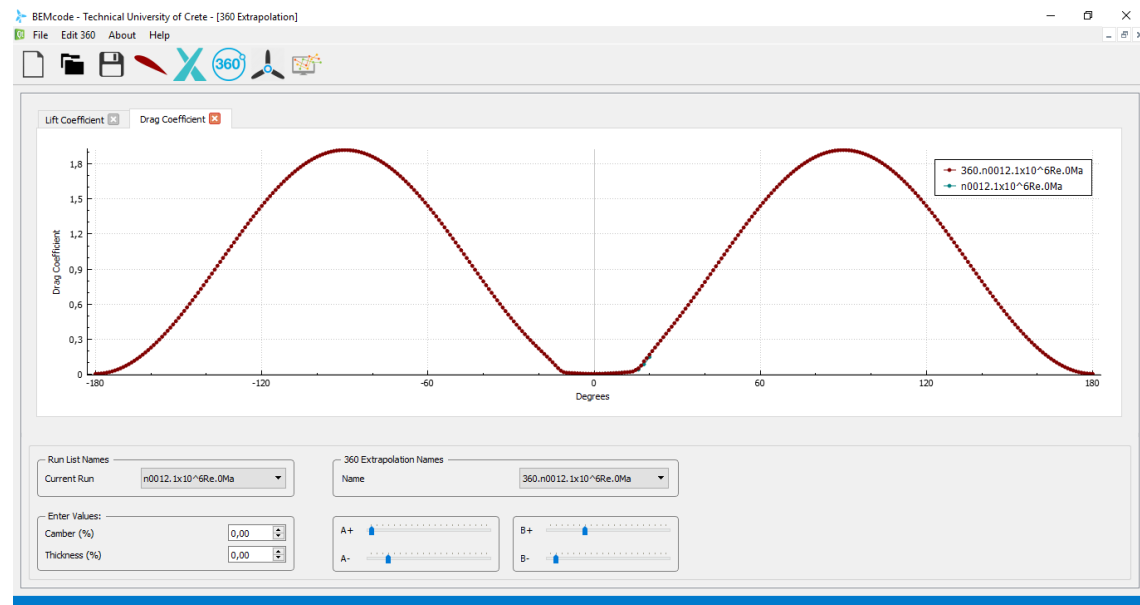


Figure 3.43: The 360° Extrapolation Drag Coefficient plot.

Additionally, the name of the 360° extrapolation is added in the 360 Extrapolation Names combo (Figure 3.44).

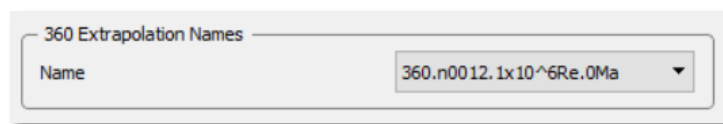


Figure 3.44: The updated 360 Extrapolation Names list.

3.6 Blade Creation Dialog

Once completing the calculations of the imported airfoils in XFOIL analysis and 360° Extrapolation dialogs, the user is able to access the **Blade** dialog in order to create the wind turbine blade. It is important to note, that in order this dialog's functions to operate accurately, all previous dialog's calculation should be completed successfully.

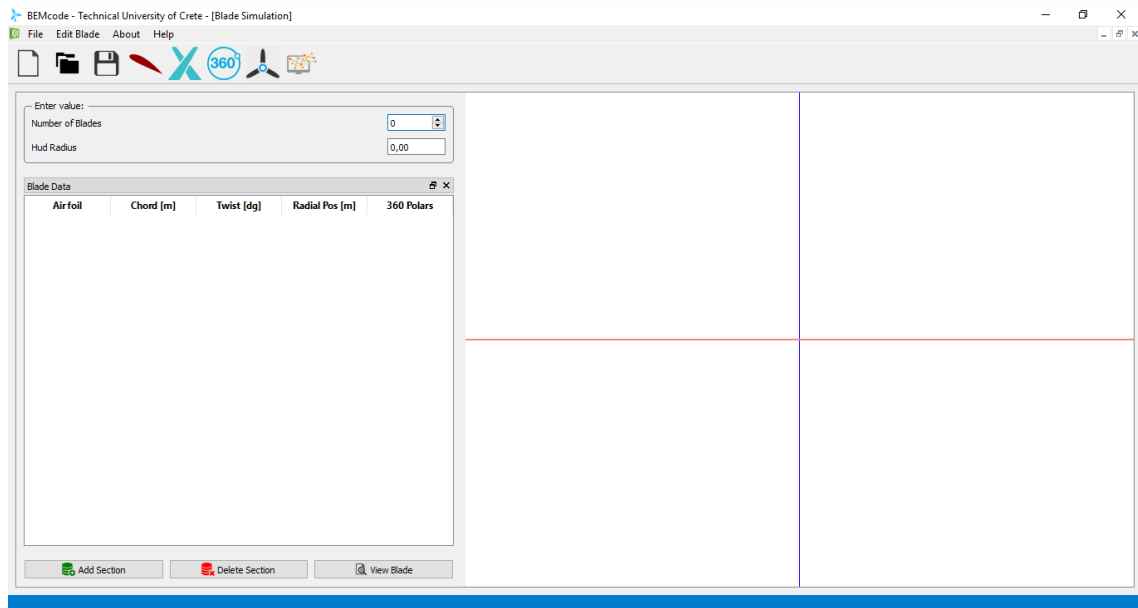


Figure 3.45: Blade creation main window.

The main window of the **Blade** dialog (Figure 3.45) is splitted in two parts. The right part is consisted of a 3-dimension area where the blade will be displayed. The left one provides the following features:

Parameters

- **Number of Blades:** The number of blades that will be previewed.
- **Hub Radius:** The hub radius (meters).



Blade Data Table

The data matrix consists of 5 columns, which are:

- Airfoil: The name of the airfoil.
- Chord [m]: The chord value (meters).
- Twist [deg]: The twist value (degrees).
- Radial Pos [m]: The radial position of the airfoil (meters).
- 360 Polars: The name of the 360° extrapolation run.



Airfoil	Chord [m]	Twist [dg]	Radial Pos [m]	360 Polars
---------	-----------	------------	----------------	------------

In order the aforementioned table to be filled with rows, the user has to press the **Add Section** button. In case one or more sections needs to be removed from the matrix, the user can select the desired row/section and then press the **Delete Section** button. Once user has added the desired number of sections, then is able to preview the blade by pressing the **View Blade** button (Figure 3.46).



Figure 3.46: Add Section, delete Section and View Blade buttons.

Edit Blade Menu

Clicking on the Edit Blade menu on the Menu Bar, the user is able to import an existed blade from the directory by selecting the option **Import Blade...** (Figure 3.47):

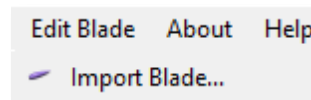


Figure 3.47: Edit Blade menu.

Blade Generation Example

In order the user to understand better the way this dialog operates, a simple example of a blade will be used. The airfoil that is going to be used is NACA 0012 and all the XFOIL and 360° extrapolation calculations have achieved as explained in previous dialogs. At first, the values of the two parameters are:

- Number of Blades = 1
- Hub Radius = 0.8 m

Inserting 4 sections for this example of blade, the data of each section as prescribed by the user are depicted in Figure 3.48.

Blade Data					
	Airfoil	Chord [m]	Twist [dg]	Radial Pos [m]	360 Polars
1	n0012	0.522	38.01	0.340	360.n0012.1x10 ⁶ f
2	n0012	0.340	15.60	0.945	360.n0012.1x10 ⁶ f
3	n0012	0.204	8.39	1.734	360.n0012.1x10 ⁶ f
4	n0012	0.127	3.00	2.702	360.n0012.1x10 ⁶ f

Figure 3.48: Example of a 4-section Blade data matrix.

Subsequently, by pressing the *View Blade* button the 3D blade is created in the plot area, as illustrated in Figure 3.49. The complete view of the *Blade Creation* window after the resulted blade is shown in Figure 3.50.

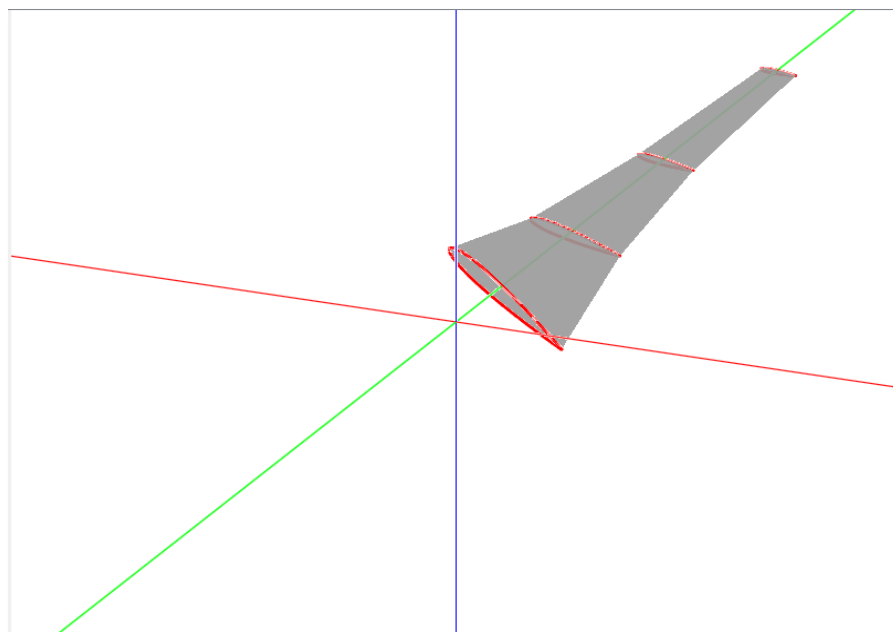


Figure 3.49: The generated blade composed by 4 airfoil sections.

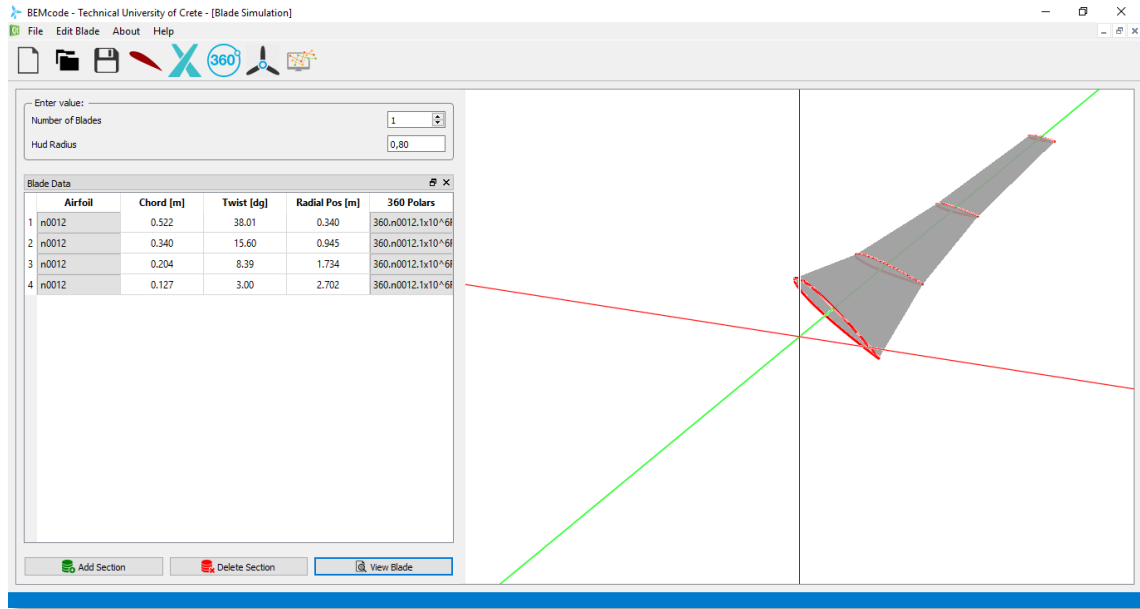


Figure 3.50: The Blade main window.

3.7 BEM Simulation Dialog

The user enters the **BEM Simulation** dialog by pressing the *BEM Simulation* button on the toolbar menu. The main window of this dialog (Figure 3.51) is splitted in two parts. The right part – BEM Simulation - is composed of multiple input data boxes while in the rest window there is a plot, on which will be resulted various data plots.

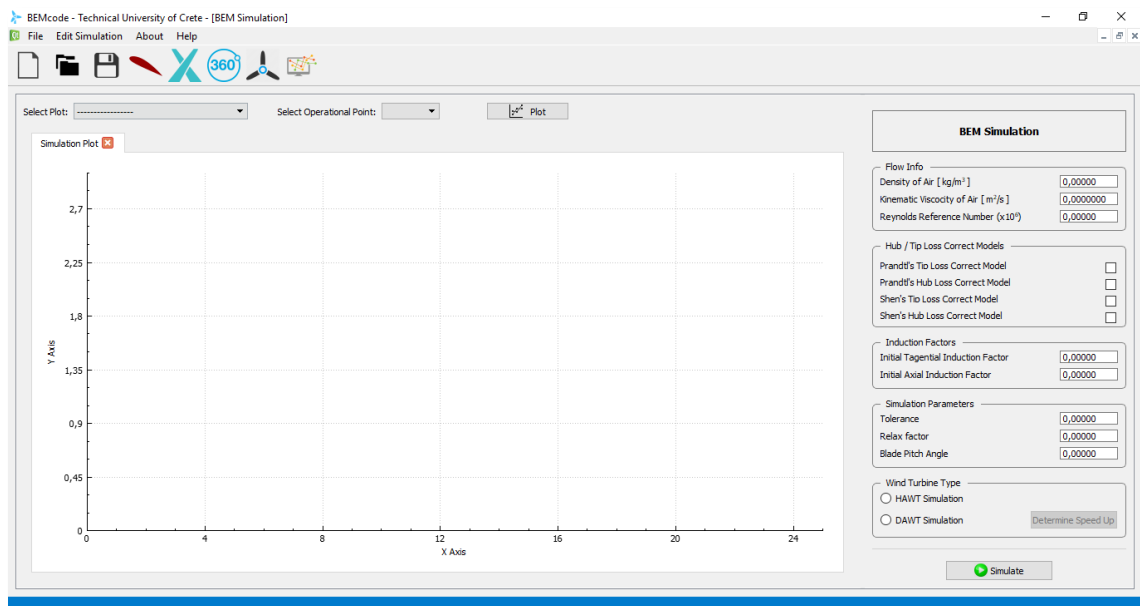
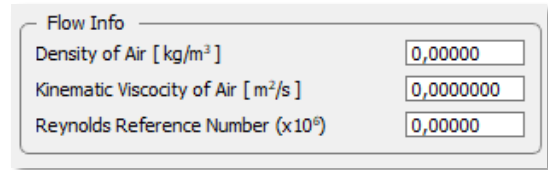


Figure 3.51: BEM Simulation main window.

The features of the *BEM Simulation* input data are the following:

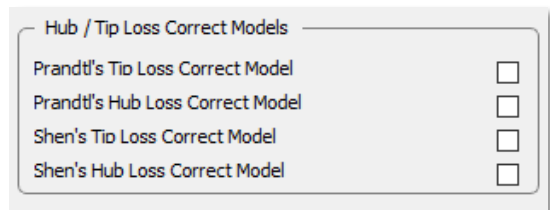
Flow Info

- Density of Air (kg/m³): The number of density of the air in kg/m³.
- Kinematic Viscosity of Air (m²/s): The number of kinematic viscosity of the air in m²/s.
- Reynolds Reference Number (10⁶): The Reynolds number.



Hub/Tip Loss Correction Models Checkboxes

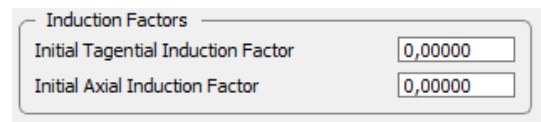
- Prandtl's Tip Loss Correction Model
- Prandtl's Hub Loss Correction Model
- Shen's Tip Loss Correction Model
- Shen's Hub Loss Correction Model



The user needs to select whose correction model will be applied in the simulation.

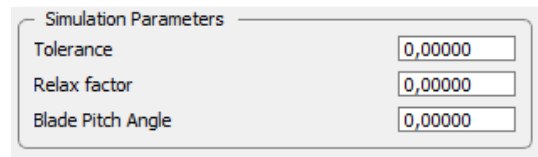
Induction Factors

- Initial Tangential Induction Factor
- Initial Axial Induction Factor



Simulation Parameters

- Tolerance: Number of tolerance.
- Relaxation factor: Number of the relaxation factor.
- Blade Pitch Angle: Number of the pitch angle.



Wind Turbine Type Radio buttons

The user has to choose if the simulation will run on a HAWT or a DAWT by pressing the radio button next to each option.

- HAWT Simulation
- DAWT Simulation



If the user selects to run the simulation on a DAWT then the **Determine Speed Up** button is enabled and the user needs to provide the value of speed-up in the **Speed-Up Distribution** table (Figure 3.52).

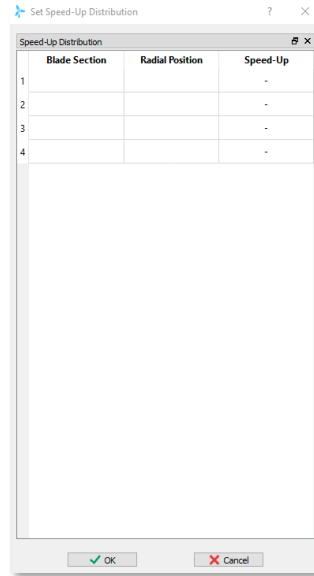
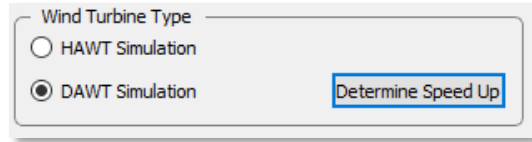


Figure 3.52: Speed Up Distribution Table (4-row example).

Subsequently, by providing values in all boxes, the user is able to proceed in by clicking on the **Simulate** button (Figure 3.53).

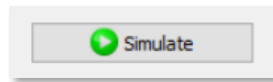


Figure 3.53: Simulate button.

Operational Points Table

A new table is shown on the window (Figure 3.54), when the user presses the *Simulate* button. At first the number of operational points needs to be defined. Subsequently, the values of wind speed (*m/s*) and the rotational speed (*rpm*) are essential in order the TSR (Tip Speed Ratio) to be automatically calculated.

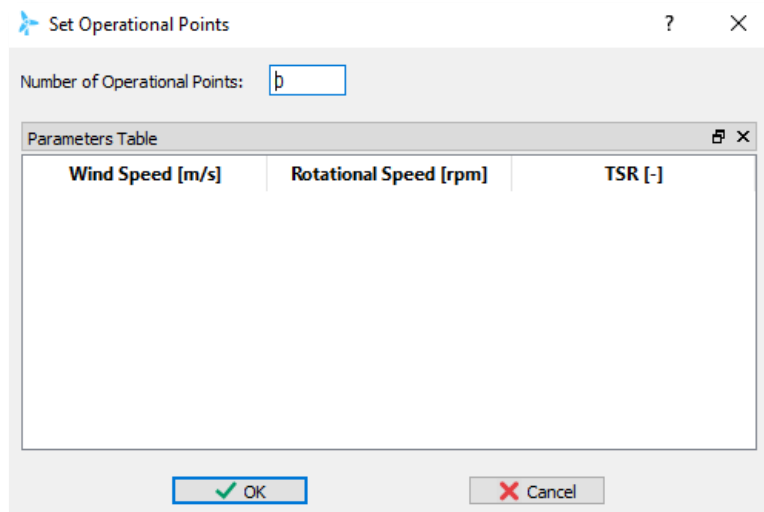


Figure 3.54: Operational Points data Table.

By pressing the *Ok* button, a message box appears on the window (Figure 3.55), informing the user that the simulation completed successfully and now the plots can be displayed.

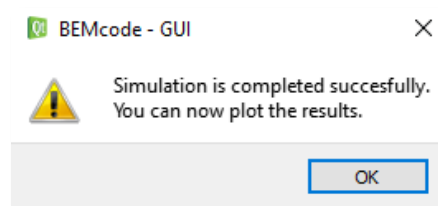


Figure 3.55: Successful Simulation - Message box.

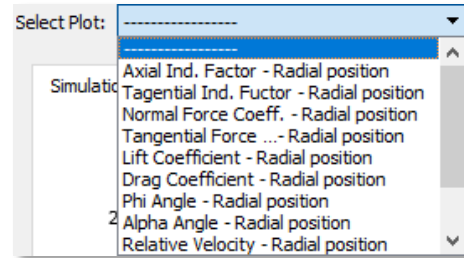
Plot Features

Plot Selection

The user is able to select one of the following plots:

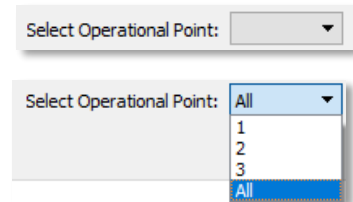
- *Axial Induction Factor - Radial Position*
- *Tangential Induction Factor - Radial Position*
- *Normal Force Coefficient - Radial Position*

- *Tangential Force - Radial Position*
- *Lift Coefficient - Radial Position*
- *Drag Coefficient - Radial Position*
- *Phi Angle - Radial Position*
- *Alpha Angle - Radial Position*
- *Relative Velocity - Radial Position*
- *Power Coefficient - Tip Speed Ratio*
- *Power Coefficient - Wind Speed*
- *Thrust Coefficient - Tip Speed Ratio*



Operational Point Selection

The number of operational points is defined by the user as shown in Figure 3.54. The selection combo-box is filled automatically and the user is able to choose which operational point is plotted. Moreover, there is the option all operational points to be plotted.



Plot Button

Once the above selections have been defined, the user can check the resulted plots by pressing the **Plot** button.



Edit Simulation Menu

It is possible the user to extract the resulted data from the plots by clicking the **Export...** option in the *Edit Simulation* menu and then selecting the desired plot name (Figure 3.56).

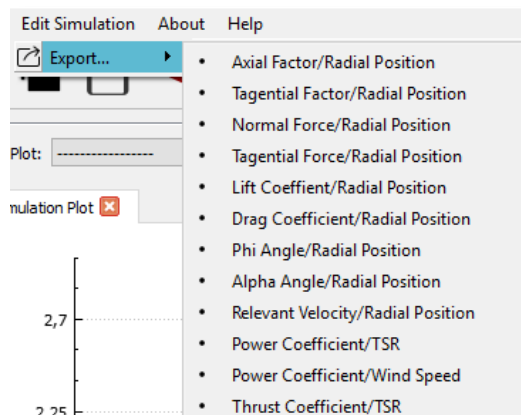


Figure 3.56: Edit Simulation menu – Export option.

Chapter 4 – Validation

In order to assess the validity of **BEMcode** software three case studies were encountered, including two HAWT rotors and one DAWT rotor. For the cases of the HAWT rotors, the results obtained from **BEMcode** were compared against those attained from the well-known QBlade code [Mar13], which is a BEM software for the analysis of wind turbine rotors, developed in Hermann Föttinger Institut of Technical University of Berlin (TUB). On the other hand, for the case of the DAWT rotor, the results obtained from **BEMcode** were compared against both experimental measurements and numerical data available in the literature.

4.1 Case I: NREL Phase VI Blade

UAE Phase VI Turbine [Lin03] is a two-bladed and S809 airfoil type wind turbine with fixed operation state of 72 rpm rotational speed and a three-degree pitch angle. The blades have a literal sweeping chord length of 0.737 m which decreases to 0.305 m and a twist angle of 20.04° at the largest chord, that fades to -2.50° at the tip, while they have a linear taper with an aspect ratio of 7.2, which is less than half the value for modern large wind turbines, providing a value of rotor's aerodynamic solidity equal to 5.8 percent. The geometry of the 5.532 m NREL Phase VI blade (Figure 4.1) utilized in UAE Phase VI turbine, as well as the analytical rotor characteristics are thoroughly described in [Lin03].

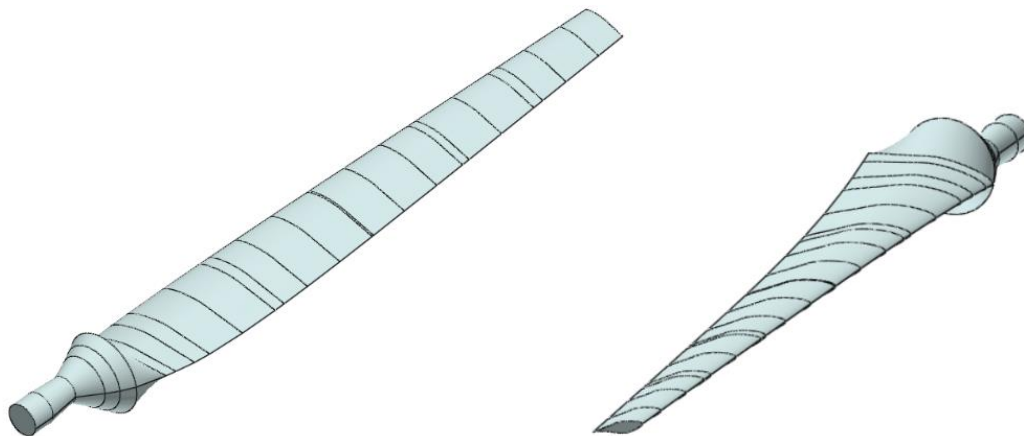


Figure 4.1: NREL Phase VI Blade Geometry.

The NREL Phase VI blade is defined by 27 airfoil sections, where the 6 first have a circular profile and the rest 21 a S809 airfoil profile. In QBlade, the user is able to choose the number of blade element as he wishes (increase in number of blade elements increases accuracy). However, for a fair comparison between the two solvers, the number of blade elements when simulating the Phase VI turbine with QBlade was also set equal to 27. The values of the other parameters used during the simulations performed with both **QBlade** and **BEMcode** are presented in Table 1.

<i>NREL Phase VI Rotor</i>	
<i>Parameter</i>	<i>Value</i>
Density of Air (ρ)	1.2250 kg/m ³
Speed of Sound	340.29 m/s
Kinematic Viscosity of Air (ν)	1.78 × 10 ⁻⁵ m ² /s
Altitude	0 m
Number of Blades (B)	2
Tip Radius (R_{tip})	5.532 m
Hub Radius (R_{hub})	0.508 m
Rotational Speed	72 rpm
Number of Sections	27
Relaxation Factor (ω_{relax})	0.3
Blade Pitch Angle	0
Tolerance (ϵ)	10 ⁻⁴
Cut in Wind Speed	5 m/s
Cut out Wind Speed	25 m/s

Table 1: Simulation parameters for the NREL Phase VI rotor.

4.1.1 Case I: Results

In Figure 4.2, the power and thrust coefficients (as a function of TSR) for the Phase VI rotor are illustrated. Apparently, a good agreement for both curves has been generally found. However, **BEMcode** seems to slightly under-predict the value of both power and thrust coefficient, in comparison with QBlade, for the values of TSR lying below 6.

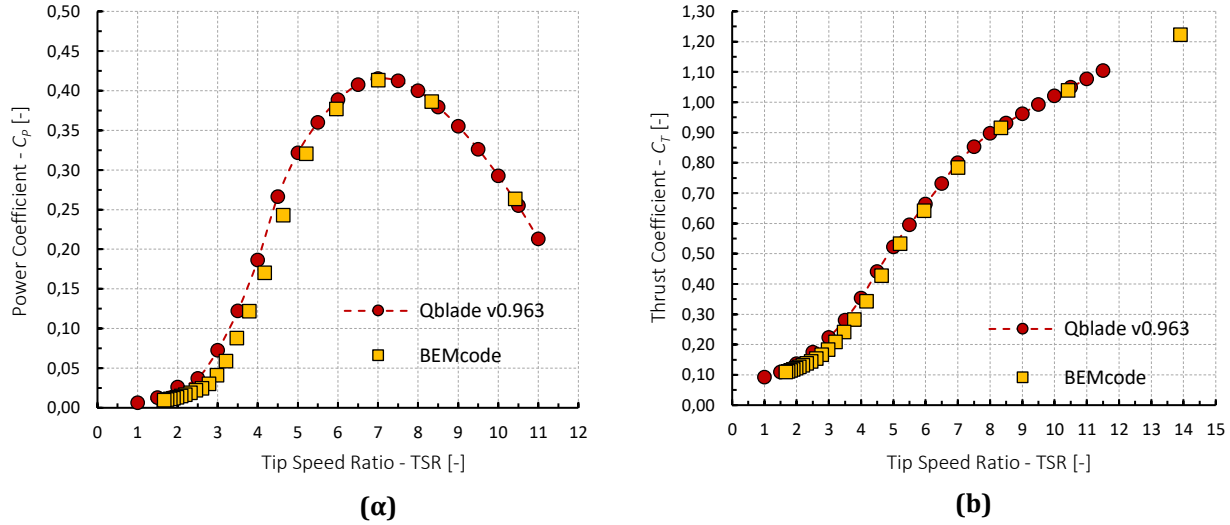


Figure 4.2: NREL Phase VI Rotor: BEMcode and QBlade data comparison for the power and thrust coefficients. (a) $C_p - TSR$. (b) $C_T - TSR$.

Through Figure 4.3 to Figure 4.6, a more detailed comparison between the results of **BEMcode** and **QBlade** is provided, by using several characteristic quantities of a BEM simulation. Overall, high levels of similarity between the results of the two software have been detected, as long as all the examined quantities are concerned. The only noteworthy discrepancies have been observed for the lift and drag coefficient distributions, regarding values of radial position between approximately 1.5 m and 3.0 m.

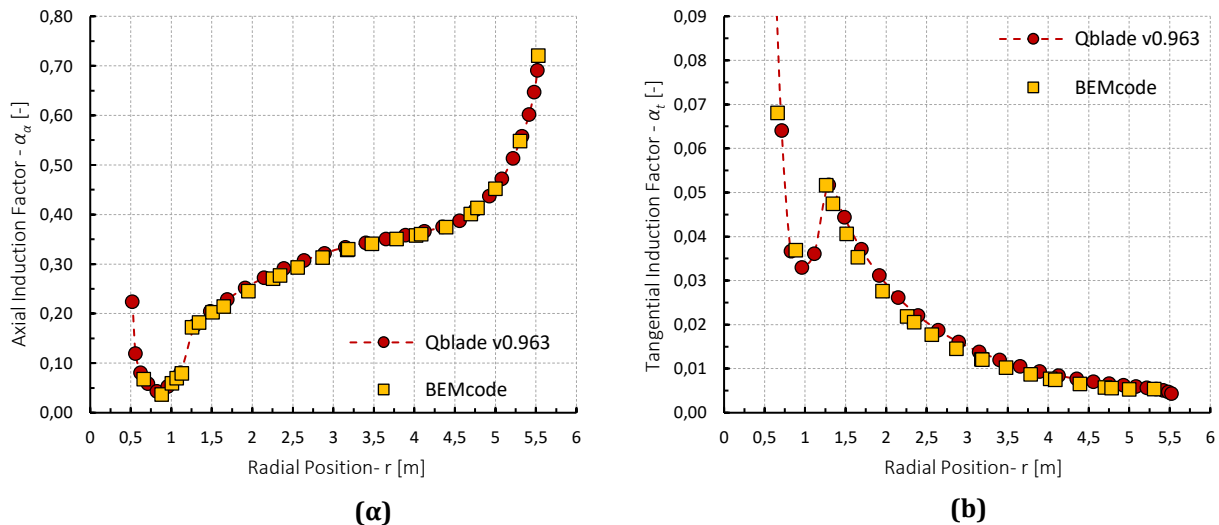


Figure 4.3: NREL Phase VI Rotor: BEMcode and QBlade data comparison for the axial and tangential induction factors. (a) $\alpha_a - r$. (b) $\alpha_t - r$.

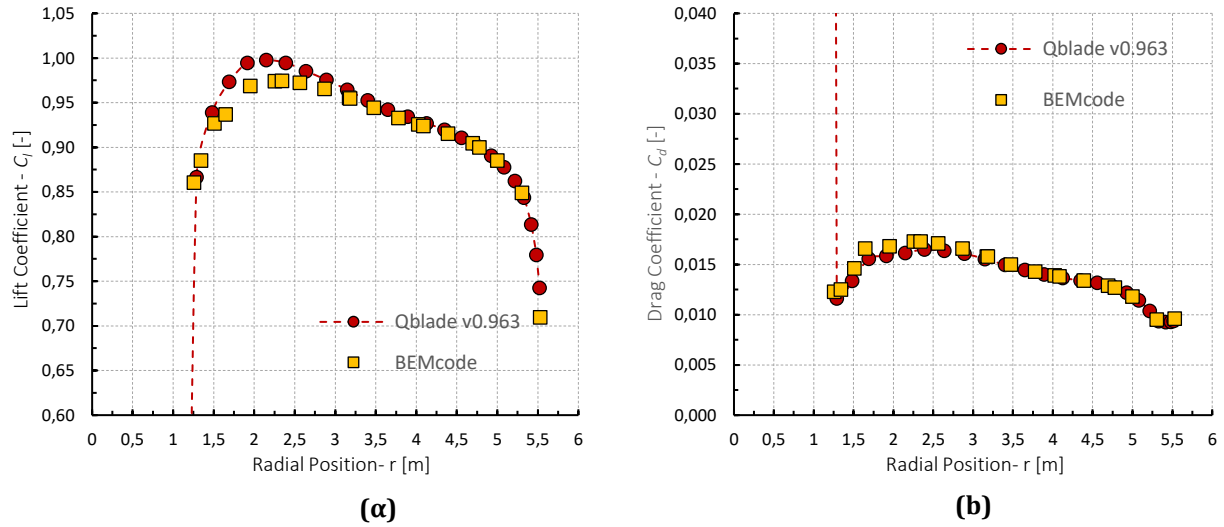


Figure 4.4: NREL Phase VI Rotor: BEMcode and QBlade data comparison for the lift and drag coefficients.

(a) $C_l - r$. (b) $C_d - r$.

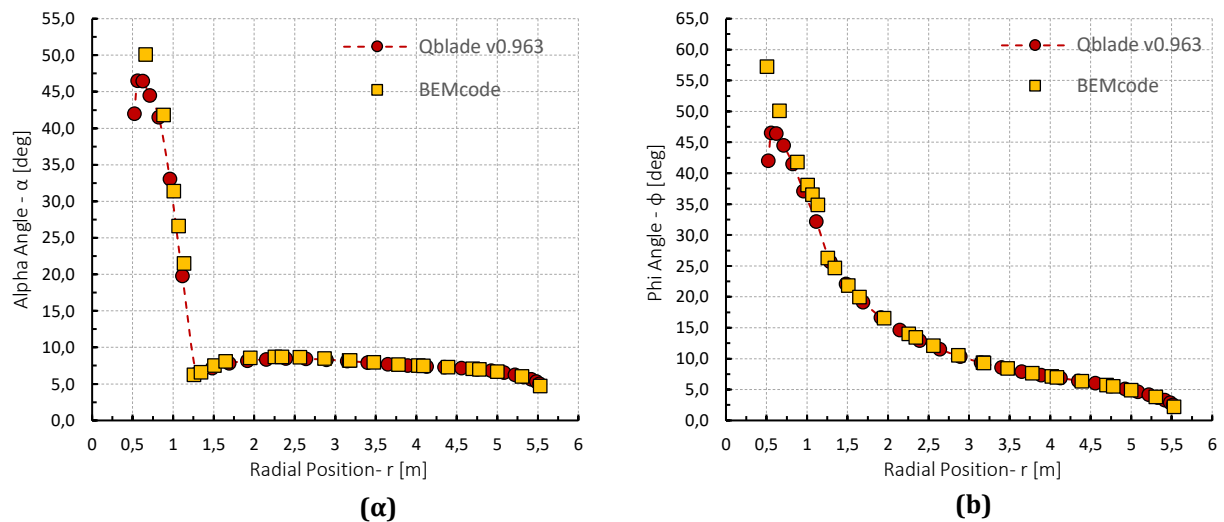


Figure 4.5: NREL Phase VI Rotor: BEMcode and QBlade data comparison for the angle of attack and the angle of the inflow velocity. (a) $\alpha - r$. (b) $\phi - r$.

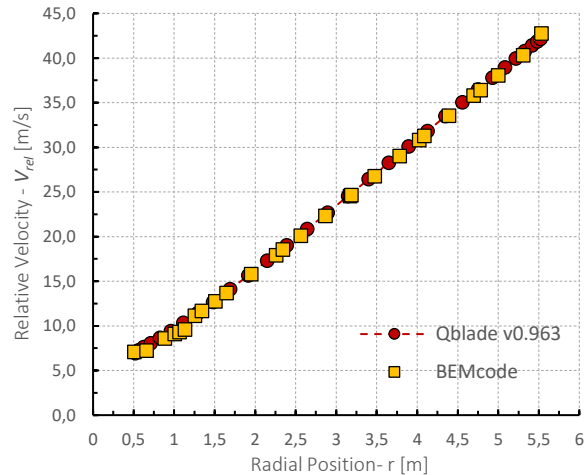


Figure 4.6: NREL Phase VI Rotor: BEMcode and QBlade data comparison for the inflow (relative) velocity magnitude.

4.2 Case II: NREL 5MW

The airfoils and chord schedule used in the development of 61.5 m models in the NREL 5MW study and also the UpWind study [UpWind12] were adopted from the DOWEC study [Koo03, Lin02]. The reported DOWEC airfoil schedule is listed in Table 2. The NREL 5MW blade is defined by 19 airfoil sections, where the 4 first have a circular profile and the rest 15 are a TU-Delft family of airfoils. In QBlade, the user is able to define the number of blade element (any increase in number of blade elements increases the accuracy). In particular, for a more accurate comparison between the two solvers, the number of blade elements set equal to 19. In Table 3, are listed the values of the other parameters necessary for the simulations performed both in **QBlade** and **BEMcode**.

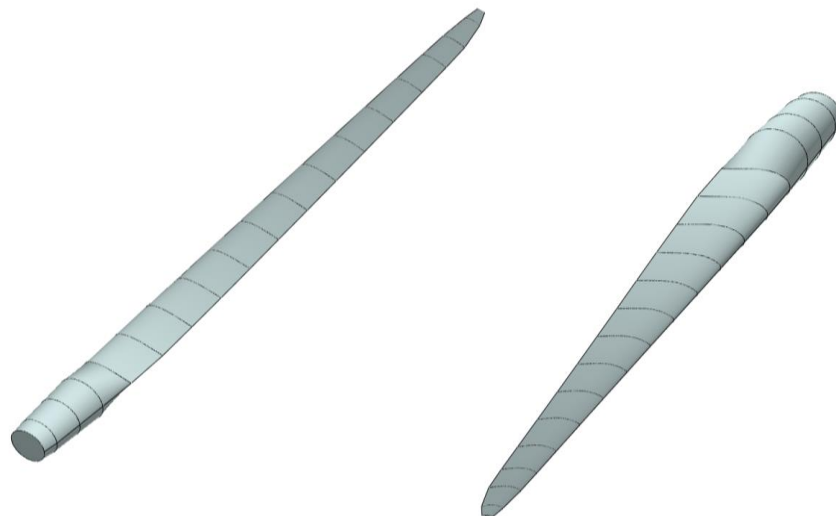


Figure 4.7: The NREL 5MW blade geometry.

NREL 5MW Blade
Circular airfoil
DU 99 W405 LM
DU 99 W350 LM
DU 97-W300 LM
DU 91-W2250 LM
DU 91-W210 LM
NACA 64618

Table 2: The airfoils composing the NREL 5MW blade..

NREL 5MW 3-Blade Rotor	
Parameter	Value
Density of Air (ρ)	1.225 kg/m ³
Speed of Sound	340.29 m/s
Kinematic Viscosity of Air (ν)	1.78 · 10 ⁻⁵ m ² /s
Altitude	0 m
Number of Blades (B)	3
Tip Radius (R_{tip})	63 m
Hub Radius (R_{hub})	1.5 m
Number of Sections	19
Relaxation Factor (ω_{relax})	0.3
Blade Pitch Angle	0
Tolerance (ϵ)	10 ⁻⁴
Cut in Wind Speed	3 m/s
Cut out Wind Speed	25 m/s

Table 3: Simulation parameters for the NREL 5MW rotor.

4.2.1 Case II: Results

In Figure 4.7, the NREL 5MW rotor’s power and thrust coefficients (as a function of TSR) are shown. In contrast with the NREL Phase VI power and thrust coefficient results, an even better agreement (for all the TSR values considered) between **BEMcode** and **QBlade** has been found for the NREL 5MW rotor:

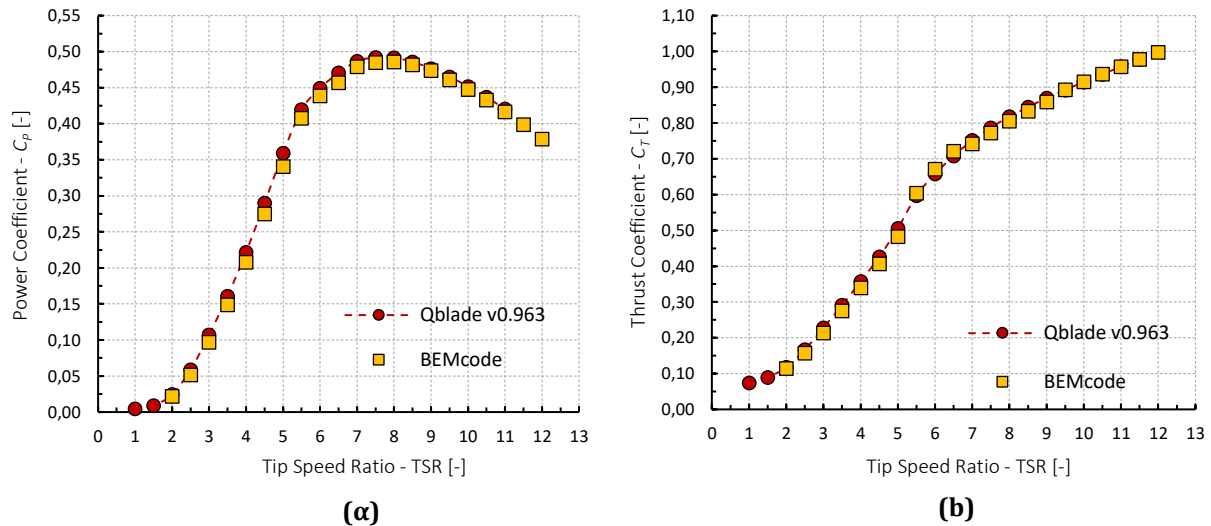


Figure 4.7: NREL 5MW Rotor: BEMcode and QBlade data comparison for the power and thrust coefficients. (a) $C_p - TSR$. (b) $C_T - TSR$.

Through Figure 4.8 to Figure 4.11, a good agreement in the compared results emerged from **QBlade** and **BEMcode** has been observed. Nevertheless, **BEMcode** appears to slightly under-predict the resulted data for values of radial position below 10 m , in comparison with **QBlade**.

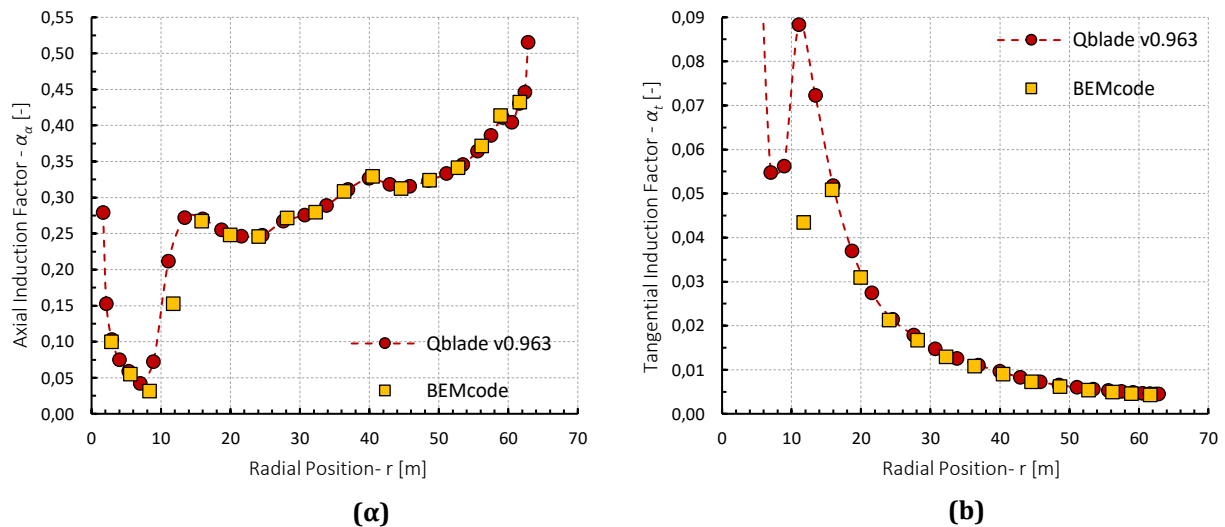


Figure 4.8: NREL 5MW Rotor: BEMcode and QBlade data comparison for the axial and tangential induction factors. (a) $a_a - r$. (b) $a_t - r$.

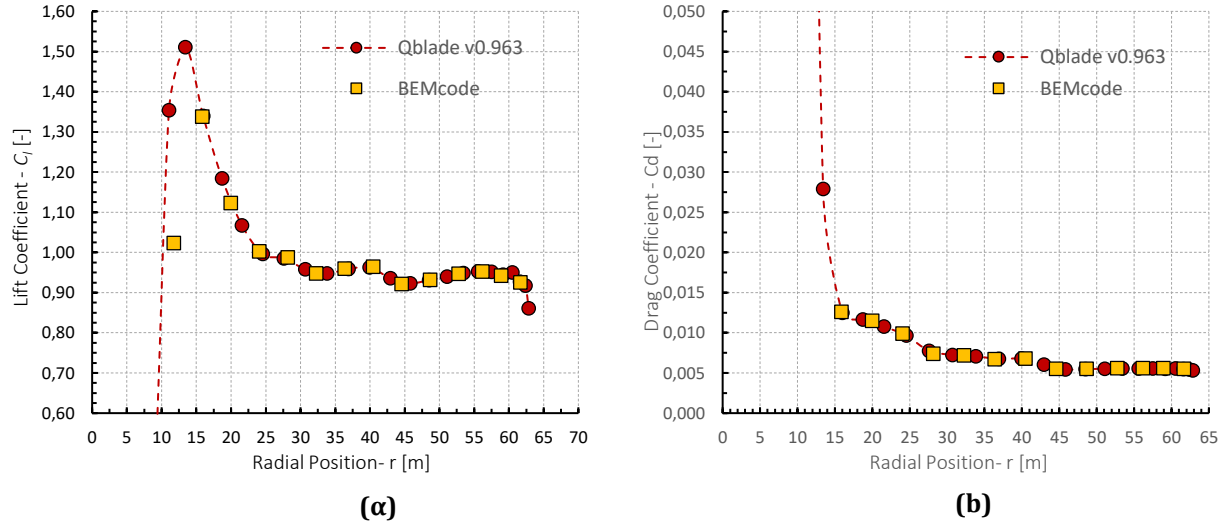


Figure 4.9: NREL 5MW Rotor: BEMcode and QBlade data comparison for the lift and drag coefficients. (a) $C_l - r$. (b) $C_d - r$.

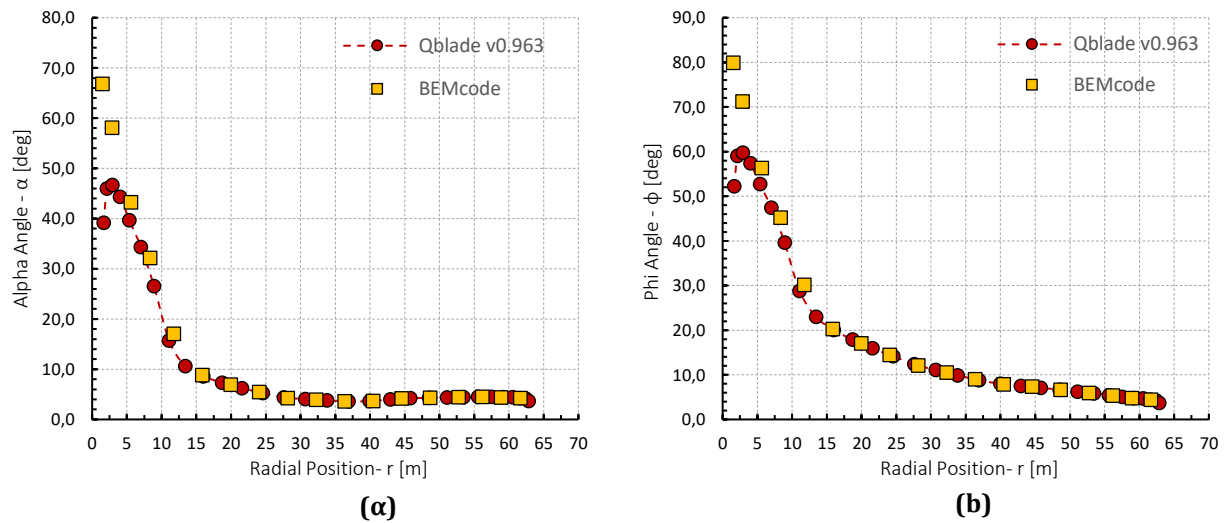


Figure 4.10: NREL 5MW Rotor: BEMcode and QBlade data comparison for the angle of attack and the angle of the inflow velocity. (a) $\alpha - r$. (b) $\phi - r$.

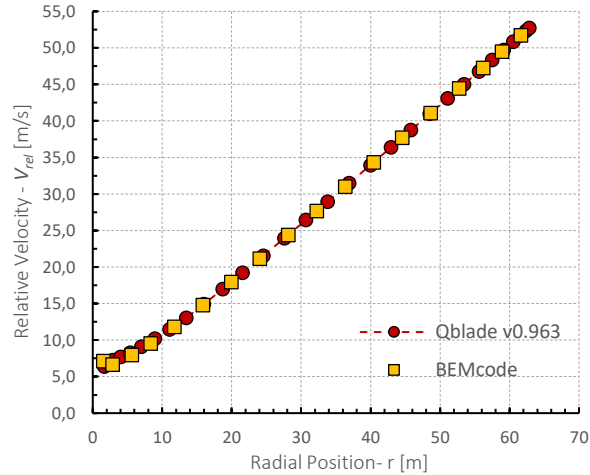


Figure 4.11: NREL 5MW Rotor: BEMcode and QBlade data comparison for the inflow (relative) velocity magnitude.

4.3 Case III: The DAWT of Donqi Urban Windmills

In this section the ability of the current BEM implementation to accurately predict the performance of DAWT rotors is assessed. For that reason, the results of BEMcode are compared against the experimental results published by van Dorst [Dor11], who conducted a series of wind tunnel measurements in an effort to design improved rotor blades for the Donqi Urban Windmills. Therefore, van Dorst examined three DAWT configurations, by using the same diffuser geometry but different blade designs. The diffuser was shaped with an exit-area-ratio (i.e., the ratio between the diffuser exit plane area and the rotor swept area) equal to 1.728, and an exit plane diameter equal to 2 m, while it was equipped with a 0.04 m high Gurney flap. The velocity speed-up γ distribution over the rotor plane for the unloaded diffuser is presented in Figure 4.12, as it was measured by van Dorst [Dor11], and numerically approximated by Kesby et al. [Ke16] through CFD simulations.

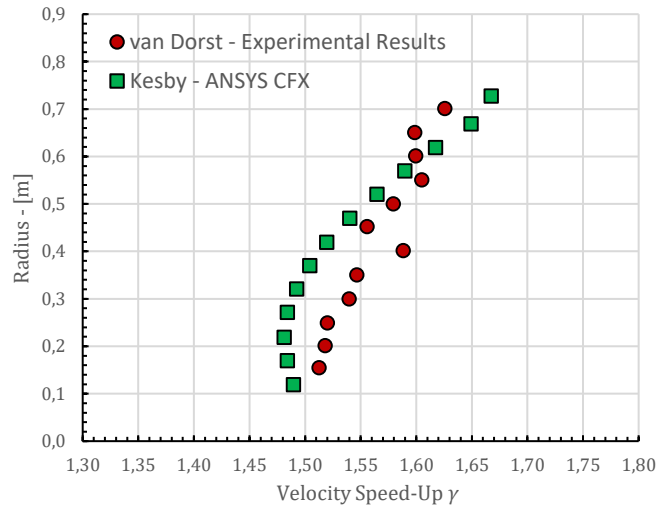


Figure 4.12: The velocity speed-up distribution over the rotor plane for the unloaded diffuser of Donqi Urban Windmills.

The three blade designs tested by van Dorst [Dor11], which are denoted as old, optimal, and linearized, are presented in Figure 4.13, mounted on the diffuser. The old blade refers to the geometry that was originally manufactured for the diffuser, based on the NACA 2207 airfoil. The optimal blade generated by a chord and twist optimization of the old blade, while the third blade was obtained by the linearization of the optimal one, in an effort to reduce the material amount and the production costs [Dor11]. Furthermore, the particular case study was also encountered by Kesby et al. [Kes16], who employed the CFD/BEM method they developed, to approximate the power output of the three DAWT rotors of radius equal to 0.75 m [Lel17].



Figure 4.13: The three blade designs mounted on the diffuser of Donqi Urban Windmills [Dor11].

4.3.1 Case III: Results

Through Figures 4.14 – 4.16, provides the experimental power output for the old, optimal and linearized blade designs, in comparison with the numerical results obtained from BEMcode and the coupled CFD/BEM method proposed by Kesby [Kes16], with and without the inclusion of the Prandtl’s tip loss correction model. Regarding the losses caused by the rotor’s 0.15 m radius hub, the Prandtl’s hub loss correction model was included in both cases. Additionally, in the current simulation, the velocity speed-up distribution, resulting from the CFD analysis of Kesby et al. [Kes16], was utilized instead of the experimental speed-up distribution measured by van Dorst [Dor11], as both the experimental and numerical speed-up distributions, presented in Figure 4.12, led to practically identical power output predictions. In this work, 7 operational points were examined, by considering a fixed rotational speed of 716.2 rpm and various values of the ambient wind speed between 5 m/s and 8 m/s.

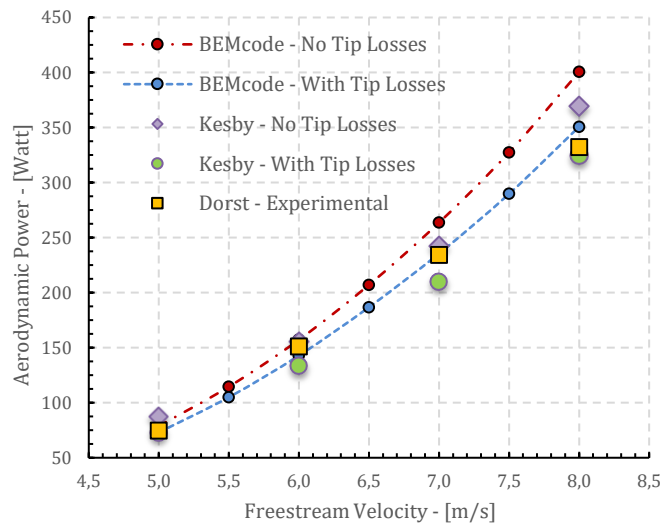


Figure 4.14: Experimental and BEMcode data comparison of the Aerodynamic Power as a function of Freestream Velocity for the DAWT configuration with the old blade (Donqi Urban Windmills case).

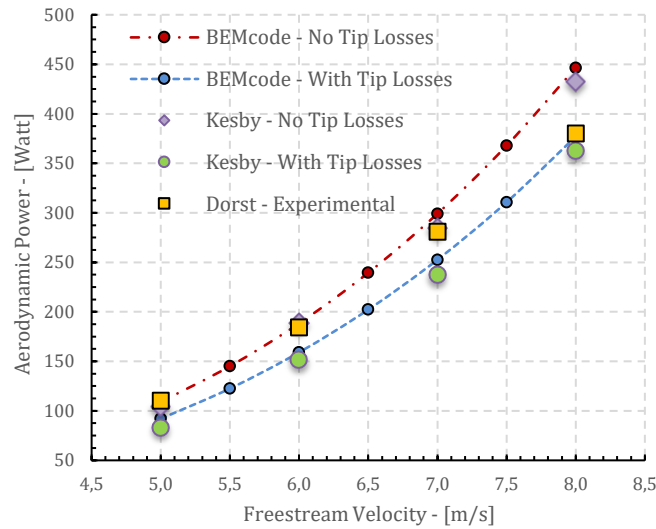


Figure 4.15: Experimental and BEMcode data comparison of the Aerodynamic Power as a function of Freestream Velocity for the DAWT configuration with the optimal blade (Donqi Urban Windmills case).

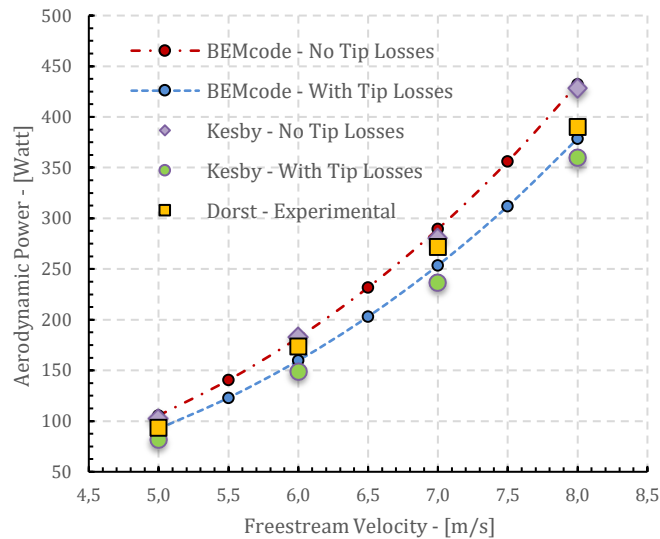


Figure 4.16: Experimental and BEMcode data comparison of the Aerodynamic Power as a function of Freestream Velocity for the DAWT configuration with the linearized blade (Donqi Urban Windmills case).

The results from BEMcode indicate a good association between the simulated and the experimental power output measurements for all the blade configurations that were examined. Nevertheless, some notable discrepancies have been detected for the case in which the Prandtl's tip loss model was not included, for freestream velocity equal to 7 m/s and 8 m/s. This highlights the importance of including such a model within the analysis, even though it generally leads to an underestimation of the power output of DAWT rotors.

Chapter 5 – Conclusions

In this Diploma thesis, a Graphical User Interface (GUI) has been developed in order to support a wind turbine analysis software (**BEMcode**), based on the Blade Element Momentum theory. The particular GUI was entirely implemented using the **C++** programming language, along with **Qt** cross-platform application. The user is able to take advantage of the different data input methods, as well as to visualize and extract the simulation results. The main modules of the GUI are the following:

- 2D Airfoil Creation and Plotting.
- XFOIL analysis.
- 360° Extrapolation of the Aerodynamic Coefficients.
- Blade Definition and Visualization.
- BEM Simulation of HAWT and DAWT rotors.

In order to assess computational part of BEMcode software three case studies were encountered in this work, including two HAWT rotors and one DAWT rotor. For the cases of the HAWT rotors, the results obtained from BEMcode were compared against those attained from the well-known QBlade code [Mar13], which is a BEM software for the analysis of wind turbine rotors, developed in Hermann Föttinger Institut of Technical University of Berlin (TUB). For the case of the DAWT rotor, the results obtained from BEMcode were compared against both experimental measurements and numerical data available in the literature.

As long as the comparison between BEMcode and QBlade is concerned, the resulting axial and induction factors distributions – as well as the distribution of other characteristic quantities – on the rotor plane from the two codes match well enough; however, some discrepancies observed, in terms of power and thrust coefficients, have to be further examined. Regarding the DAWT rotor simulation, the obtained results from BEMcode demonstrated a good agreement with experimental data, while indicated that the utilization of the Prandtl's tip loss correction is still desirable during the analysis of DAWTs, especially as the value of the freestream velocity increases. However, a possible underestimation of the actual power output should be anticipated.

In general, the behavior of BEMcode is rendered very satisfying, given that more correction models and features are planned to be incorporated, so as to render the code stable and accurate for different turbine configurations.

References

- [And08] Anderson, J.D., *Fundamentals of Aerodynamics*, McGraw-Hill, 5th edition, 2008.
- [Bet13] Betz, A., 2013, "The Maximum of the Theoretically Possible Exploitation of Wind by Means of a Wind Motor", *Wind Engineering*, **37**(4), pp. 441–446.
- [Buh05] Buhl, M. L., 2005, *A New Empirical Relationship between Thrust Coefficient and Induction Factor for the Turbulent Windmill State*, Tech. Report NREL/TP-500-36834, National Renewable Energy Laboratory.
- [Bus07] Van Bussel, D. G. J. W., 2007, "The Science of Making More Torque from Wind: Diffuser Experiments and Theory Revisited", *Journal of Physics: Conference Series*, 75.
- [Dor11] van Dorst, F. A., 2011, *An Improved Rotor Design for Diffuser Augmented Wind Turbine*, M.Sc. Thesis, Faculty of Aerospace Engineering, Delft University of Technology.
- [Gla26] Glauert, H., *The Elements of Airfoils and Airscrew Theory*, Cambridge University Press, 1926.
- [Han15] Hansen, M.O.L., *Aerodynamics of Wind Turbines*, Earthscan from Routledge, Third edition, 2015.
- [Hol81] Van Holten, T., "Concentrator Systems for Wind Energy, with Emphasis on Tipvanes" *Wind Engineering*, Vol. 5, No. 1, 1981, pp. 29-45.
- [Igr81] Igra, O., "Research and Development for Shrouded Wind Turbines", *Energy Conversion and Management*, Vol. 21, 1981, pp. 13–48.
- [Kes16] Kesby, J. E., Bradney, D. R., and Clausen, P. D., 2016, "Determining Diffuser Augmented Wind Turbine Performance Using a Combined CFD/BEM Method", *Journal of Physics: Conference Series*, 753.
- [Koo03] Kooijman, H. J. T., Lindenburg, C., Winkelaar, D., and van der Hooft, E. L., 2003, *DOWEC 6 MW Pre-Design: Aero-elastic modeling of the DOWEC 6 MW pre-design in PHATAS*, Energy Research Center of the Netherlands: ECN-CX--01-135, DOWEC 10046_009.
- [Lan07] Lanzafame, R., Messina, M., 2007, "Fluid dynamics wind turbine design: Critical analysis, optimization and application of BEM theory", *Renewable Energy*, Vol. 32, pp. 2291–2305.
- [Lel15] Leloudas, S.N. and Nikolos, I.K., 2015, "Development of a Blade Element Momentum (BEM) code for rotor analysis", Intermediate Report-1, Technical University of Crete, 2015.
- [Lel16] Leloudas, S.N. and Nikolos, I.K., 2016, *A Revised Blade Element Momentum (BEM) Analysis of the 3-Blade Rotor*, Intermediate Report-10, Technical University of Crete.
- [Lel17] Leloudas, S.N., Lygidakis, G.N. and Nikolos, I.K., "Assessment of a Modified Blade Element Momentum Methodology for Diffuser Augmented Wind Turbines", *Proceedings of the ASME 2017 International Mechanical*

Engineering Congress and Exposition, Volume 7: Fluids Engineering, Tampa, Florida, USA, November 3–9, 2017, ISBN: 978-0-7918-5842-4.

[Lel18] Leloudas, S.N., Strofylas, G.A. and Nikolos, I.K., “Aerodynamic Shape Optimization of Diffuser Augmented Wind Turbine Blades Using Asynchronous Parallel Differential Evolution”, *Proceedings of the 9th GRACM International Congress on Computational Mechanics*, Chania, Greece, June 4-6, 2018.

[Lin02] Lindenburg, C., 2002, *Aeroelastic Modeling of the LMH64-5 Blade*, Energy Research Center of the Netherlands: DOWEC-02-KL-083/0, DOWEC 10083_001.

[Lin03] Lindenburg, C., 2003, *Investigation into rotor blade aerodynamics*, ECN Rep. ECN-C-03-025.

[Liu12] Liu, S., Janajreh, I., 2012, “Development and application of an improved blade element momentum method model on horizontal axis wind turbines”, *International Journal of Energy and Environmental Engineering*, Vol. 3, pp. 1–10.

[Mah06] Maheri, A., Noroozi, S., Toomer, C. A., Vinney, J., 2006, *Damping the fluctuating behavior and improving the convergence rate of the axial induction factor in the BEMT-based aerodynamic codes*, University of West England, Bristol.

[Mar13] Marten, D., Wendler, J., 2013, QBlade Guidelines, <http://www.q-blade.org/>

[She05] Shen, W. Z., Mikkelsen, R., Sørensen, J. N., Bak, C., 2005, “Tip loss corrections for wind turbine computations”, *Wind Energy*, Vol. 8, pp. 457–475.

[Sne95] Snel, H., Schepers J. G., 1995, *Joint Investigation of Dynamic Inflow Effects and Implementation of an Engineering Method*, ECNC- 94-107.

[Ton07] Tonio Sant, *Improving BEM-based Aerodynamic Models in Wind Turbine Design Codes*, Delft University, PhD Thesis, 2007.

[UpWind12] “*The UpWind Project*,” <http://www.upwind.eu>

[Vaz14] Tavares Dias do Rio Vaz, D. A., Amarante Mesquita, A. L., Pinheiro Vaz, J. R., Cavalcante Blanco, C. J., and Pinho, J. T., 2014, “An Extension of the Blade Element Momentum Method Applied to Diffuser Augmented Wind Turbines”, *Energy Conversion and Management*, Vol. 87, pp. 1116–1123.

[IEA] <https://www.iea.org/>

[UN19] <https://population.un.org/wpp/>

[WEO18] International Energy Agency (IEA), “*World Energy Outlook 2018 (WEO2018)*”.